# Field measurements of vertical suspended sand concentration profiles in the surfzone in Egmond aan Zee, the Netherlands

*Msc thesis Earth Surface and Water,*

*Track: Coastal dynamics and River systems*

*Second version: 10-02-2015*


| | |
|---|---|
| Name student: | Laura Taal |
| Student number: | 3345122 |
| 1st supervisor: | Prof. dr. B.G. Ruessink |
| 2nd supervisor: | Prof. dr. M.G. Kleinhans |


Universiteit Utrecht

## Abstract

The interaction of nearshore waves and currents are the dominant forcing to cross-shore sand transport on sandy beaches. In the nearshore surf zone, suspended sediment transport attributes a significant amount of the total transport. The distribution of suspended sand concentration depends on the complex interactions between waves and currents. A good understanding of the time-averaged vertical suspended sediment concentration profile is important in sediment transport calculations. In this study, the influence of hydrodynamics and bedforms on vertical suspended sand concentrations profiles under field conditions is analyzed. Measurements of time-averaged vertical suspended sediment concentration profiles with associated hydrodynamics and bedforms were made in the surf zone near Egmond aan Zee in October 2013. The vertical suspended sediment concentration profiles were measured with 7 optical backscatter sensors placed on top of each other. The bedform configuration was measured using a 3D ripple scanner. Conflicting to models from literature, results show that the shape of the vertical suspended sand concentration in the surfzone was independent on neither hydrodynamics nor bedform type. All vertical suspended sand concentration profiles, reference concentrations and eddy diffusivities showed similar values for all types of bedforms and hydrodynamic conditions. This may be caused due to the time lag effects in bedform development. Under calm weather conditions, when environmental conditions were not dynamic enough, bedforms can not adjust instantaneously with the hydrodynamic changes. This provides higher sediment concentrations than expected. This tidal asymmetry may have major effects for modelling suspended sand transport in the surf zone.

-

# Contents

# 1 Introduction

The surf zone is the most dynamic region with highest sediment transport rates at a time scale of few seconds to decades. One of the aspects within the study of sediment transport is research on vertical Suspended Sand Concentration profiles (hereafter: vertical SSC profiles). An accurate calculation of time-averaged vertical suspended sand concentration is crucial for understanding suspended sand entrainment and transport processes. Since the 1950's, extensive research is being done on sand transport (Van Rijn, et al., 2013). A recent overview of studies on sediment transport and vertical SSC profiles can be read in for example Davies and Thorne (2008). Environmental conditions in the surfzone change continually due to nonlinear interactions between hydrodynamics and bedforms. It is still unclear which factors affect suspended sand concentration and to what extent (Thorne, et al., 2002).

In particular, bedforms provide different sand entrainment mechanisms, resulting in a wide range of models for vertical SSC profiles. With modern technology, these bedforms can be measured with increased accuracy allowing improved SSC studies on the combination of hydrodynamic parameters and different bedform types. Since 2013, the department of physical geography at Utrecht University has obtained a sonar 3D ripple scanner which measures ripple configurations in 1 $m^2$ areas in three dimensons. This 3D scanner provides an excellent opportunity to study ripple formation and corresponding vertical SSC profiles.

In October 2013, field measurements were conducted in the surfzone near Egmond aan Zee. The reporting of this fieldwork is divided into two studies:

1. Research on bedforms (Schrijvershof, 2014).
2. Research on vertical suspended sand concentration profiles.

This thesis focus on vertical SSC profiles in the surfzone with water depths between 1 – 3 meters. The ripple data is analyzed in study 1 (Schrijvershof, 2014). Results from study 1 are used in this study without any adjustments.

The most common approach to model vertical SSC profiles is an exponential solution of the diffusion equation and a power-law developed by Rouse (1937). Both models depend on a near-bed concentration which determines the magnitude of the vertical SSC profile and a shape-parameter which determines the steepness. Since it is still unclear which parameters influence

vertical SSC profiles and to what extent, this study will investigate the influence of hydrodynamics and bedforms on vertical SSC profiles.
The answer to this question will be investigated by the following sub-questions:

1. Hydrodynamics
    a. Which hydrodynamic parameters control the magnitude of suspended sand concentration?
    b. Which hydrodynamic parameters influence the shape of the vertical SSC profile?
2. Bedforms
    a. What is the influence of different bedforms on the magnitude of suspended sand concentration?
    b. What is the effect of different type of bedforms on the shape of vertical SSC profiles?

This thesis will continue with a theoretical review on the influence of hydrodynamics and bedforms in chapter 2. The setup of the fieldwork, data processing and selection are described in the methods (chapter 3). The field campaign results and vertical SSC profiles data analysis are described in chapter 4. In the discussion (chapter 5), results are compared with literature studies and the effect of relaxation time will be discussed. The conclusions are stated in chapter 6.

# 2 Literature review

## 2.1 Background information

Suspended sand creates the largest portion of sand transport in the surfzone (Van Rijn, 1993) and it can be assumed that breaking waves and processes in shallow water always cause enough turbulence for sand to get in suspension. Sand remains in suspension when the upward and downward forces are equal (Figure 1).This vertical balance, averaged over several wave periods, can be described by the following diffusion equation:

$$w_s \bar{c} + \epsilon_s \frac{d\bar{c}}{dz} = 0 \qquad (2.1)$$

Where:

| | | | |
|---|---|---|---|
| $\bar{c}$ | = time averaged volume concentration at height z above the bed | | $[kg\ m^{-3}]$ |
| $z$ | = height above sea bed | | $[m]$ |
| $w_s$ | = fall velocity | | $[m\ s^{-1}]$ |
| $\epsilon_s$ | = sand diffusivity | or sand mixing coefficient | $[m^2 s^{-1}]$ |

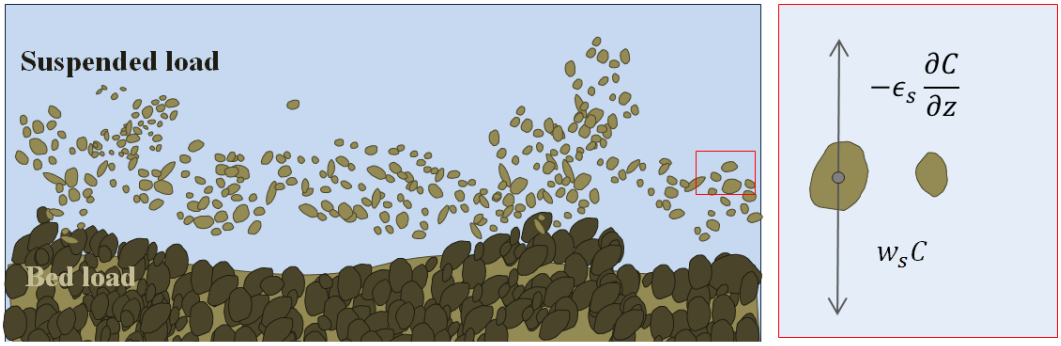


**Figure 1: Bed load and suspended load. Right: Schematization of the diffusion equation with the upward eddy diffusivity forces and downward fall velocity.**

Assuming that only diffusion plays a role and no advection, the vertical SSC profile in the nearshore zone can be described by the analytically solved first-order linear differential equation of eq. (2.1). The concentration $C(z)$ at elevation $z$ above the bed is:

$$C(z) = C_0 e^{P_{diff}} \qquad (2.2)$$

With $P_{diff}$:

$$P_{diff} = \frac{w_s}{\epsilon_s} z$$

Another common solution for the vertical SSC profile is the classic formulation introduced by Rouse (1937):

$$C(z) = C_0 \left( \frac{h - z}{z} \frac{z_0}{h - z_0} \right)^{P_{Rouse}} \quad (2.3)$$

With the Rouse number $P_{Rouse}$:

$$P_{rouse} = w_s / \kappa u_*$$

Where:

| | | | |
|---|---|---|---|
| $C(z)$ | : | Time averaged sand concentration at height z above the bed | $[gl^{-1}]$ |
| $C_0$ | : | Reference concentration | $[gl^{-1}]$ |
| $h$ | : | Water depth | $[m]$ |
| $z_0$ | : | Reference bed level | $[m]$ |
| $\kappa$ | : | Von Karmen constant = 0.4 | $[-]$ |
| $u_*$ | : | Bed-shear velocity | $[ms^{-1}]$- |

These two equations can be extended with advection (e.g. Van Rijn, 1993) or statistical components (e.g. Zheng et al., 2013), but because of their ease of use and comprehensibility the exponential equation (2.2) and the Rouse equation (2.3) are the commonly used equations to solve suspended sand concentration at height $z$ in the water column (Van Rijn, 1993). Both equations express that suspended sand concentration is highest down near the sea bed at the source and decreases higher up in the water column depending on two major unknowns: the power $P$ and the reference concentration $C_0$. These two variables determine the shape of the vertical SSC profile. The reference concentration represents the 'start signal' and magnitude of the concentration. The power $P$, also called *shape* or *Rouse parameter*, determines the steepness of the vertical SSC profile.

Many descriptions for $P$ and $C_0$ ranging from simple to complex, can be found in literature. The following paragraphs present an overview of factors influencing vertical SSC profiles, based on several examples in previous studies. This overview is not exhaustive, but it supports the basic principle shown in figure 2: the value of $P$ and $C_0$ depends on a nonlinear interaction between suspended sand, hydrodynamics and bedforms and no single process can describe the variability in concentration magnitude.

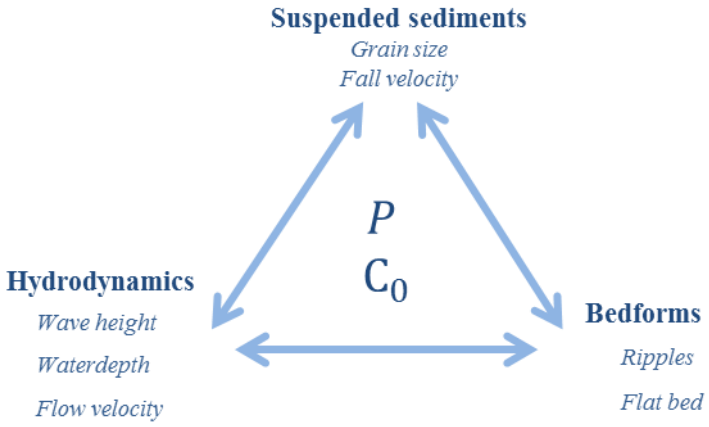


**Figure 2: The interacting 'sand triad' showing the relationship between hydrodynamics, bedforms and suspended sands (after: Davies & Thorne, 2008).**

## 2.2 Suspended sand

The amount of suspended sand transport strongly depends on particle size (Van Rijn, 2007). The sand grain size is a precondition for sand entrainment: if the available sand is too large and thus too heavy, no sand suspension occurs. The fall velocity $w_s$ is an expression for the downward force on suspended sand due to gravity. One broadly used method to calculate this fall velocity has been developed by Van Rijn (1993):

$$1 < D_{50} \leq 100\ \mu m \qquad w_s = \frac{(s-1)gD_{50}^2}{18\nu} \tag{2.4}$$

$$100 < D_{50} \leq 1000\ \mu m \qquad w_s = \frac{10\nu}{D_{70}}\left(\sqrt{1 + \frac{0{,}01(s-1)gD_{50}^3}{\nu^2}} - 1\right) \tag{2.5}$$

$$D_{50} > 1000\ \mu m \qquad w_s = 1.1\sqrt{(s-1)gD_{50}} \tag{2.6}$$

Where:

| | | | |
|---|---|---|---|
| $\nu$ | : | Kinematic viscosity | $[m^2 s^{-1}]$ |
| $D_{50}$ | : | $50^{th}$ percent of the grain diameter | $[m]$ |

Naturally, more upward force is required (whether or not in the form of turbulence) for large grains to remain in suspension compared to smaller grains. Therefore, fine sands can brought up higher in the water column. This low fall velocities (= small grains) in turn causes much steeper vertical SSC profiles for small grains comparative to high fall velocities in the same

hydrodynamic conditions (Figure 3.b). The increase in steepness of vertical SSC profiles with decreasing grain size is studied for example by Zheng et al. (2013). They studied the influence of different grain sizes on the vertical SSC profile under the same hydrodynamic conditions with mean cross-shore velocity $\bar{u} = 1\ {}^{m}/_{s}$ and ${}^{z_0}/_{h} = 0.01$. An exponential vertical SSC profile was deduced based on the diffusion equation (2.1) expressed as:

$$C(z) = C_0 e^{A\left(z^{\frac{1}{6}} - z_0^{\frac{1}{6}}\right)} \quad \text{(2.7.a)}$$

$$A = -\frac{\bar{u}\omega}{u_*(w_s + 2V_e)(\kappa h)^{\frac{1}{6}}} \quad \text{(2.8.b)}$$

$$V_e = \frac{u_*}{\sqrt{2\pi}} e^{-\frac{1}{2}\left(\frac{w_s}{u_*}\right)^2} \quad \text{(2.9.c)}$$

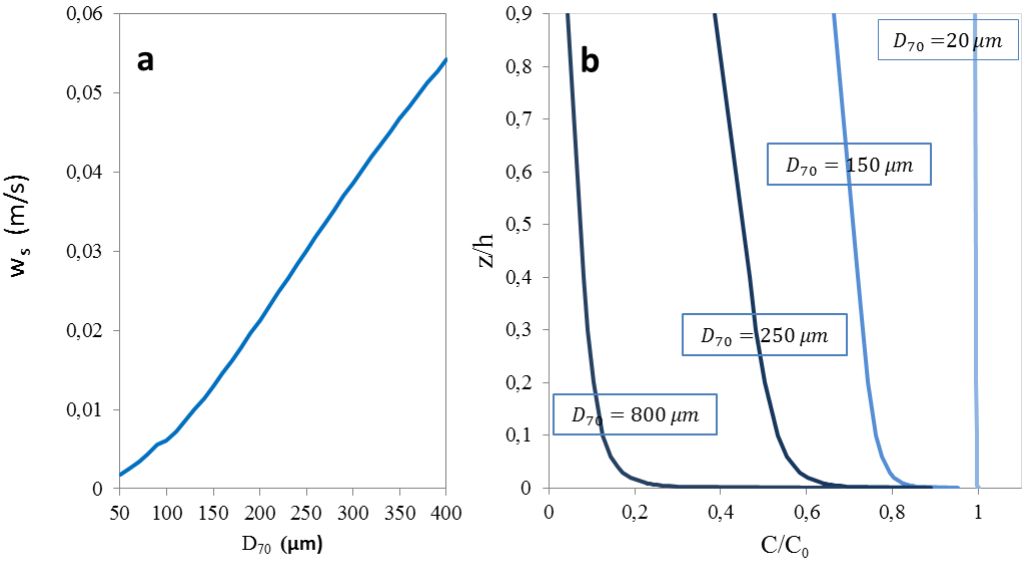


**Figure 3, a: Van Rijns method to calculate fall velocity, fall velocity increases with increasing grain size; b: Vertical SSC profile variation with sand size for the same hydrodynamic conditions with $\bar{u} = 1ms^{-1}$ and ${}^{z_0}/_{h} = 0.01$ after Zheng et al. (2013).**

## 2.3 Hydrodynamics

The surfzone is affected by both waves and tide-currents and currents generated by wave breaking. Both flows have their own vertical velocity distribution in the water column and induce bottom friction differently (Figure 4). This friction is generated in the bottom boundary layer, a thin layer where the flow slows down due to friction caused by the bed. Due to the high frequency shift in velocity of waves, the boundary layer generated by waves can not develop fully over the water column but to a few centimeters (Nielsen, 1993; Soulsby, 1997; Van Rijn,

1993, 2007). This creates a large gradient in flow velocity near the bed which induces high shear stresses causing disturbance and sand stirring near the bed. Under relatively constant flow, the current boundary layer can develop over a larger range in the water up to the total water depth (Nielsen, 1993; Soulsby, 1997; Van Rijn, 1993, 2007). Generally in coastal areas where both waves and current occur, waves are very effective in stirring the sand and currents drives sediment transport. Through these different flow mechanisms, the wave-current boundary layer can be split in two sections: the near bottom linear wave-dominated layer and logarithmic current-dominated upper layer (Van Rijn, 1993).

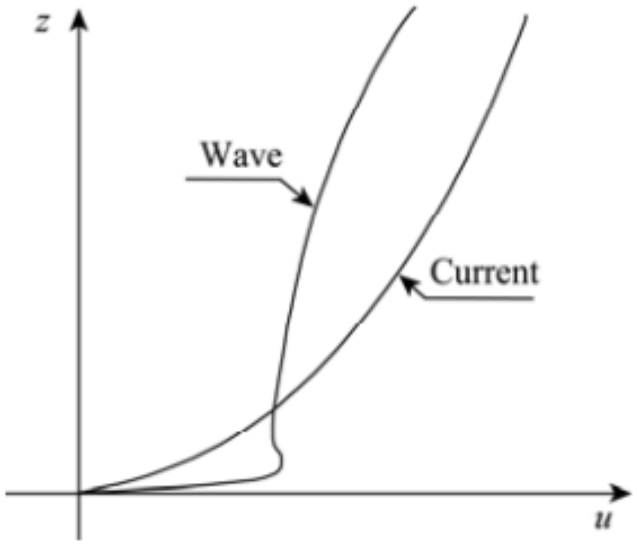


**Figure 4: Velocity distriction in wave and current boundart layers (Nielsen, 1992).**

The thickness of the bottom boundary layer and hence the strength of the bed shear stress is dependent on a complex interaction between waves and currents. The ratio between these hydrodynamic forces is often expressed as the non-dimensional shear stress $\theta$ (Nielsen, 1992). The general formula for the Shields parameter is:

$$\theta = \frac{\tau}{g(\rho_s - \rho_w)d} \qquad (2.10)$$

Where:

| | | | |
|---|---|---|---|
| $\tau$ | : | Bed shear stress | $[Pa]$ |
| $d$ | : | Grain diameter | $[m]$ |
| $\rho_s$ | : | Grain density | $[kg\ m^{-3}]$ |
| $\rho_w$ | : | Water density | $[kg\ m^{-3}]$ |
| $g$ | : | Acceleration due to gravity | $[m\ s^{-2}]$ |

The Shields parameter can be calculated for waves, currents or a combination thereof. In all cases the Shields parameter increases with higher energetic conditions, i.e.: high waves experience higher Shields parameters compared to low waves. Fluid velocities, whether generated by waves or currents, enhance the bed shear stress and therefore move and suspend larger amounts of sand (Figure 5). Besides strong currents, also wave breaking add extra bed shear stress due to turbulence generated by the wave breaking intensifies bed shear stresses. This results in large sand clouds above the seabed (Aagaard & Hughes, 2013).

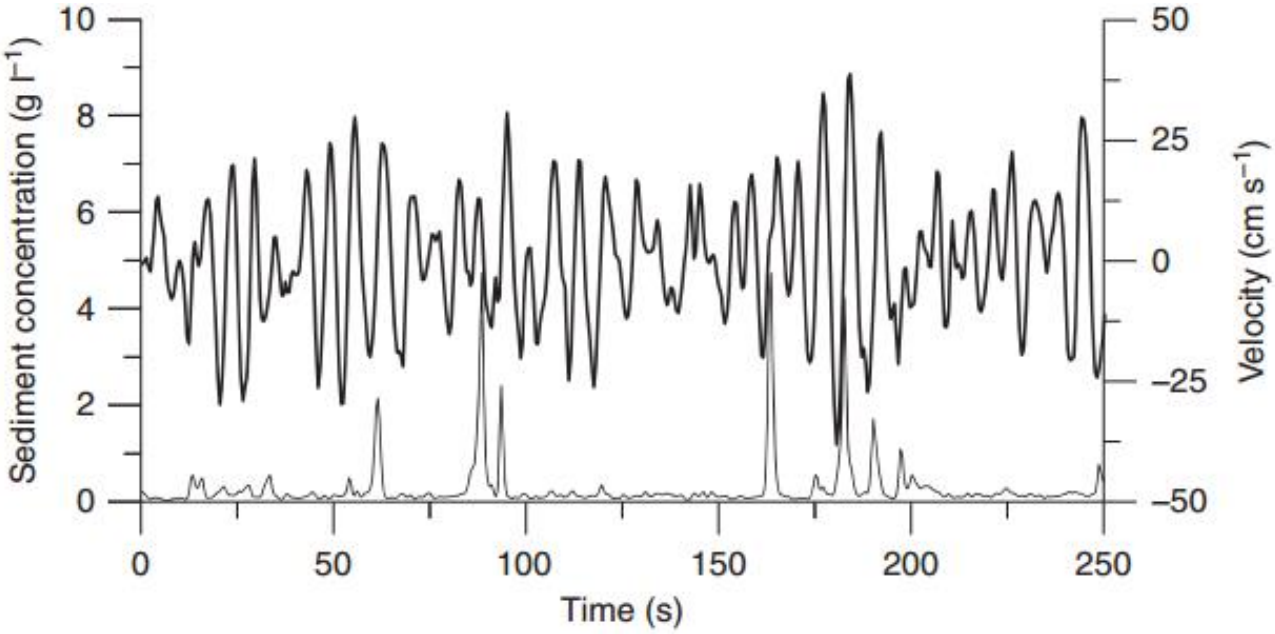


**Figure 5: Time series of cross-shore velocity (thick line) and suspended sand concentration at 5 cm above the bed (thin line). Measurements are recorded at the Danish North Sea Coast with h=7.6 m and H =1.32 m (Aagaard & Hughes, 2013).**

Different shapes and steepness of the vertical SSC profile can be seen in figure 6. The vertical SSC profiles in figure 6 are measured under semi-real conditions in the Delta Flume of Deltares Delft Hydraulics, the Netherlands (240 m long, 5 m wide and 7 m deep). This figure shows that vertical SSC profiles become steeper with increasing wave heights (= increasing bottom shear stess). However, bedforms were dynamic within hydrodynamic conditions. Therefore, the ripple type was not constant during all experiments. This demonstrates that steeper vertical SSC profiles do not simply correlate with wave height only, but depends on a combination of hydrodynamics and bedforms.

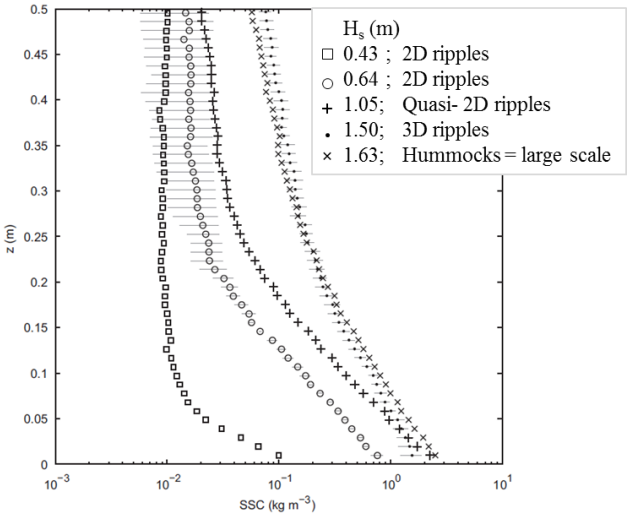


**Figure 6: Time-mean suspended sand concentration against height above the bed (O'Hara Murray, et al., 2012).**

## 2.4 Bed profile

The thickness of the bottom boundary layer determines to which extent the sediment can be stirred up. Besides the hydrodynamics (previous section), the thickness is also influenced by the configuration and size of the bedforms (Nielsen, 1986; Grant & Madsen, 1986; Camenen, 2009). At high energetic conditions, flat bed regime prevails with high sediment concentrations in a sheet layer near the bed. This sheet layer can evolve from millimeters to a few centimeters from the bottom (Dong, et al., 2013). The suspended sand decreases rapidly after this thin sheet layer compared to a gradually decrease at a rippled bed (Ribberink et al., 2000, Figure 7).

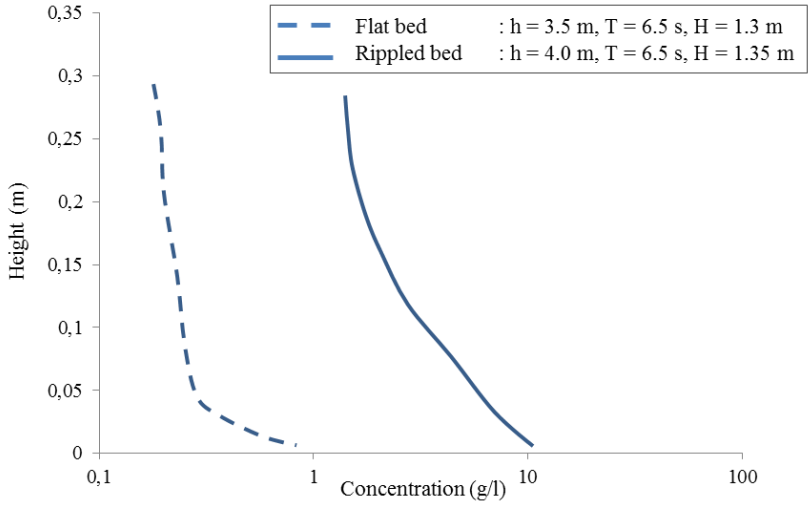


-

**Figure 7: figure from (Huisman, 2009) after (Ribberink, et al., 2000). The vertical SSC profile at flat bed decreases rapidly with increasing height above the bed.**

Sand ripples are formed when near-bed velocities are relatively small. Bedforms can surface a broad range of scales and each type modifies sand entrainment differently (Bolaños, et al., 2012). Ripple types can be classified on the basis of the wave and current Shields parameter (e.g. Arnott & Southard, 1990; Van Rijn, 1993; Amos & Li, 1999 and Van Rijn et al., 2005). Each combination of wave and current Shields parameters provides a different ripple type. For example: for low wave Shields parameters and intermediate current shields parameters, 2D/3D current dunes occur (Figure 8). A schematic overview is given in Figure 8.

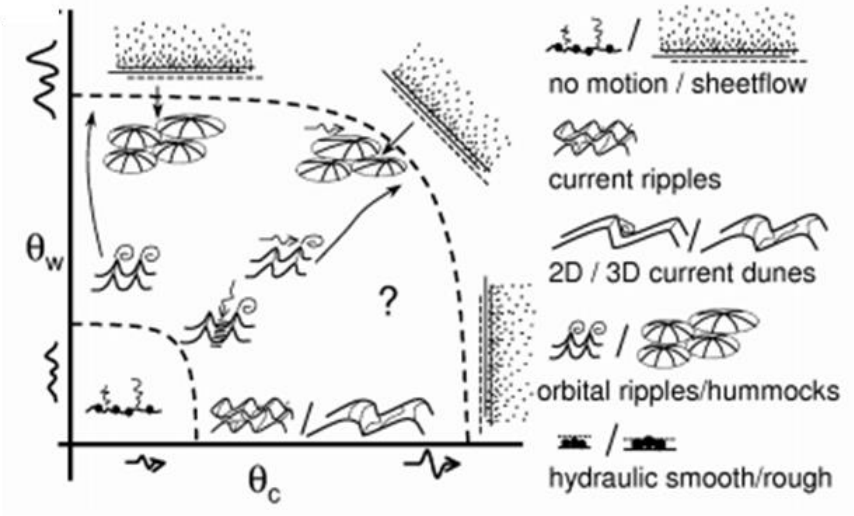


**Figure 8: Bedform stability diagram after Kleinhans (2005). The wave Shields parameter (vertical axis) is plotted against the current Shields parameter (horizontal axis). For each wave-current interaction different bedform states exist.**

Each ripple type causes its own bed roughness (Figure 9). Li and Amos (1998) classified ripple types based on this bed roughness by:

$0.75 > u_{*W}/u_{*C}$ = Current-dominant bedforms

$0.75 < u_{*W}/u_{*C} < 1.25$ = Combined wave and current bedforms

$1.25 < u_{*W}/u_{*C} < 2$ = Wave dominant bedforms

$u_{*W}/u_{*C} > 2$ = Pure wave bedforms

This difference in bed shear stress per ripple type results in different sand entrainment arising different vertical SSC profiles (e.g. Nielsen, 1992; Soulsby, 1997 and Camenen, 2009, (Thorne, et al., 2009)). For example, Vortex ripples have an ejecting character which ensures high sand concentrations even in quiet environmental conditions with a low Shields parameter (Soulsby,

1997). In the case of vortex ripples, ejection also plays a role besides diffusion (2.1). The steeper the ripple, the higher sand get ejected in the water column (Van der Werf, et al., 2008).

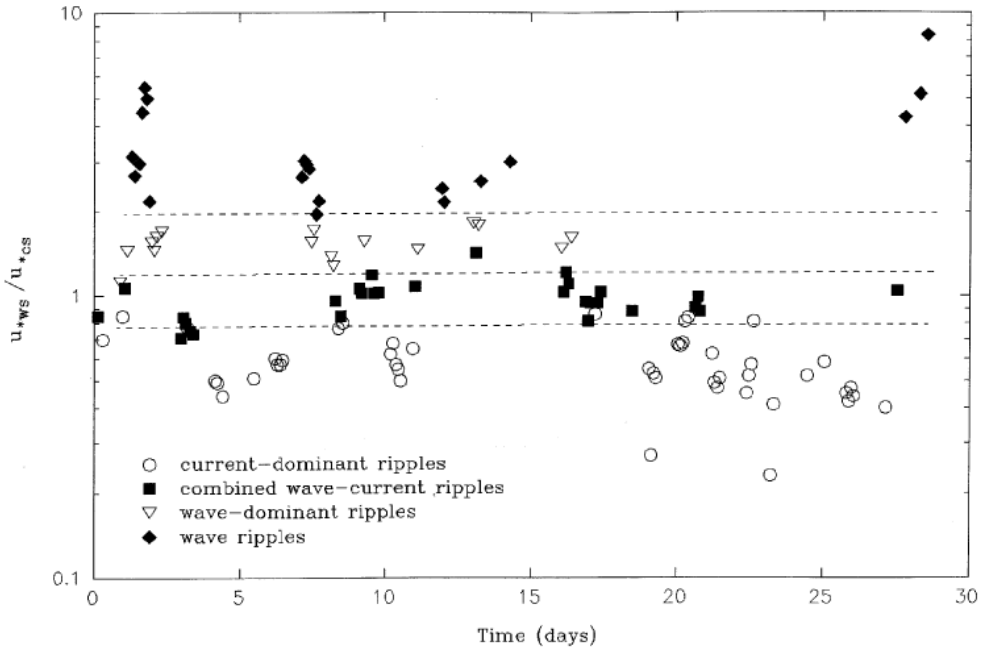


**Figure 9: The ratio of wave and current bed shear stress $u_{*w}/u_{*c}$ plotted as a function of time for selected bursts. Different ripple types generate different bed shear stress ratios. The highest ratios are generated by pure wave ripples (diamonds), followed by dominant wave ripples (triangles), combined wave-current ripples (squares) and current ripples (circles). After Li & Amos (1998).**

### *Orientation with respect to the shoreface*

Besides the ripple division on the basis of bottom friction parameters, ripples can also be divided on the basis of location along the shoreface (Figure 10). In the breaker zone, there is so much turbulence resulting in flat bed conditions. At these flat bed circumstances, concentrations are high near the bed and decreases rapidly with increasing height above the bed (left vertical SSC profiles, Figure 10). This provides less steep vertical SSC profiles compared to profiles in the zone after wave-breaking with rippled bedforms (middle vertical SSC profiles, Figure 10). In the swash zone, again flat bed conditions prevail with relatively high near-bed sand concentrations. However, the total amount of sediment is much less compared to the breaker zone since the energetic conditions are much lower.

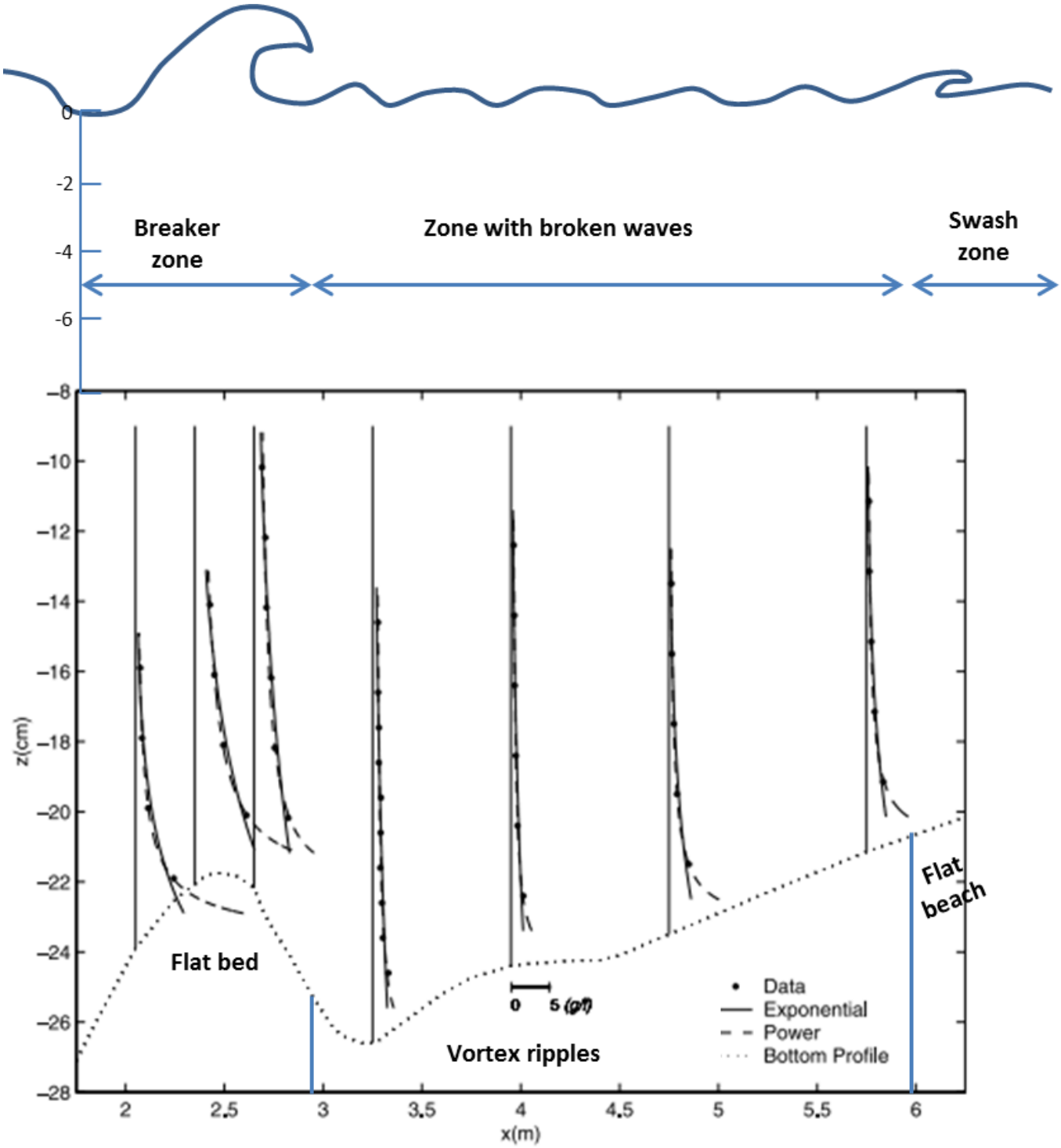


**Figure 10: Measured and fitted mean SSC profiles at different cross shore locations. Figure after (Nielsen, 1992) and (Kobayashi, et al., 2005).**

The relative wave height can help with classifying waves in different zones along the shoreface:

$$relative\ wave\ height = H_{1/3}/h \quad (2.11)$$

Where:

| | | | |
|---|---|---|---|
| $H_{1/3}$ | : | Wave height | $[m]$ |
| $h$ | : | Water depth | $[m]$ |

The value of the relative wave height depends on the beach slope, making the distinction in breaking and not-breaking flexible. From field experience the following values are assumed (Masselink, et al., 2007):

Non-breaking waves: $0.4 > {H_{1/3}}/{h}$

Breaking waves: $0.4 < {H_{1/3}}/{h} < 0.5$

Broken waves: ${H_{1/3}}/{h} > 0.5$

## 2.5 Reference concentration

Previous paragraphs briefly described sand, hydrodynamics and bedform influences on vertical SSC profiles. Each (nondimensional) parameter is a piece of information in the complex puzzle of vertical SSC profiles. However, it is quite difficult to solve this problem due to the interaction between the parameters involved. The ambition of these studies on vertical SSC profiles is to develop a representative model which to improve existing models of suspended sand transport along the coast. The exponential and Rouse equation, being the commonly used models for vertical SSC profiles, must be adjusted for the two unknown parameters of the reference concentration $C_0$ and shape parameter $P$ for them to apply.

The magnitude of the suspended sand concentration is for a large part determined by the near-bed concentration (Lee et al., 2004; Kleinhans et al., 2005; Dolphin & Vincent, 2009).

For each type of ripple or environment (deep, shallow, breaking zone), different descriptions for reference concentration have been developed. If the ripple configuration is unknown, or in flatbed situations, measured reference concentrations are extrapolated to bedding height $z = 2D_{50}$. This is also called the Nikuradse roughness length $k_s$ (Van Rijn, 1984). When the ripple configuration is known, reference concentrations are calculated with equations depending on ripple height and

length. An example of a reference concentration calculation depending on ripples can be described by an equation of Nielsen (1986):

$$C_0 = \delta \rho_s \theta_r^{3\prime} \tag{2.12}$$

Where:

$\rho_s$ : Sand density $[kg\ m^{-3}]$

$\delta$ : $5 \cdot 10^{-3}$

$\theta_r$ : Enhanced Shields parameter for a rippled bed, which is related to the wave Shields parameter $\theta_w$ by:

$$\theta_r = \frac{\theta_w}{\left(1 - \frac{\pi\eta}{\lambda}\right)^2} \tag{2.13}$$

Where:

$\eta$ : Ripple height $[m]$

$\lambda$ : Ripple length $[m]$

A more general method for calculating reference concentrations is of the form:

$$C_0 = \alpha \rho \theta^{\beta} \tag{2.14}$$

Where $\alpha$ and $\beta$ are two empirical constants. Many expressions of this form exist each depending on different factors such as environment, ripple type (eq.2.11), hydrodynamics etc., as developed by, for example: Dolphin and Vincent (2009), who found different expressions for reference concentration depending on ripple type (Figure 11).

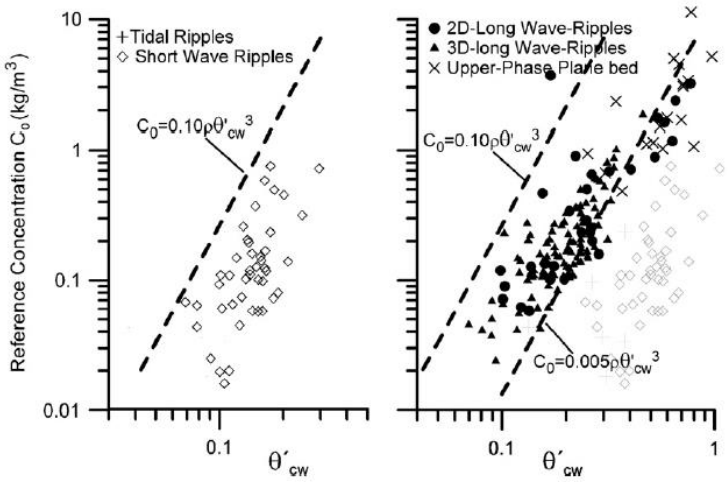


**Figure 11: Different descriptions for reference concentrations depending on ripple type. Symbols represent measured reference concentrations and dashed lines represent the best fit (Dolphin & Vincent, 2009).**

## 2.6 Shape parameter

The other unknown in the exponential equation and Rouse equation is the shape parameter $P$ which determines the steepness and shape of the vertical SSC profile. The general formula is $P = {}^{w_s}/_{\epsilon_s} z$. Within this power, the eddy diffusivity ($\epsilon_s$) describes the turbulence in the water column as a function of bottom stress, settling velocity and turbulence which stirs the sand (Camenen & Larson, 2008). As many equations exist for the reference concentration, many different equations also exist for eddy diffusivity. Still there is no consensus on a correct description (Grant & Madsen, 1979; Nielsen, 1992; Thorne et al., 2009). Descriptions of $\epsilon_s$ can be divided into the categories constant, linear and parabolic (Figure 12). The function type to calculate eddy diffusivity depends, as with reference concentrations, on ripples, hydrodynamics and sand properties (Van Rijn, 1984). Constant eddy diffusivities can be found within the bottom boundary layer (Van Rijn, 1993). When diffusion dominates, eddy diffusivity increases linearly (Dolphin and Vincent, 2009). Under combined waves and currents a parabolic function describes the eddy diffusivity profile (Coffey and Nielsen, 1987; Sistermans & Van der Graaff, 1999).

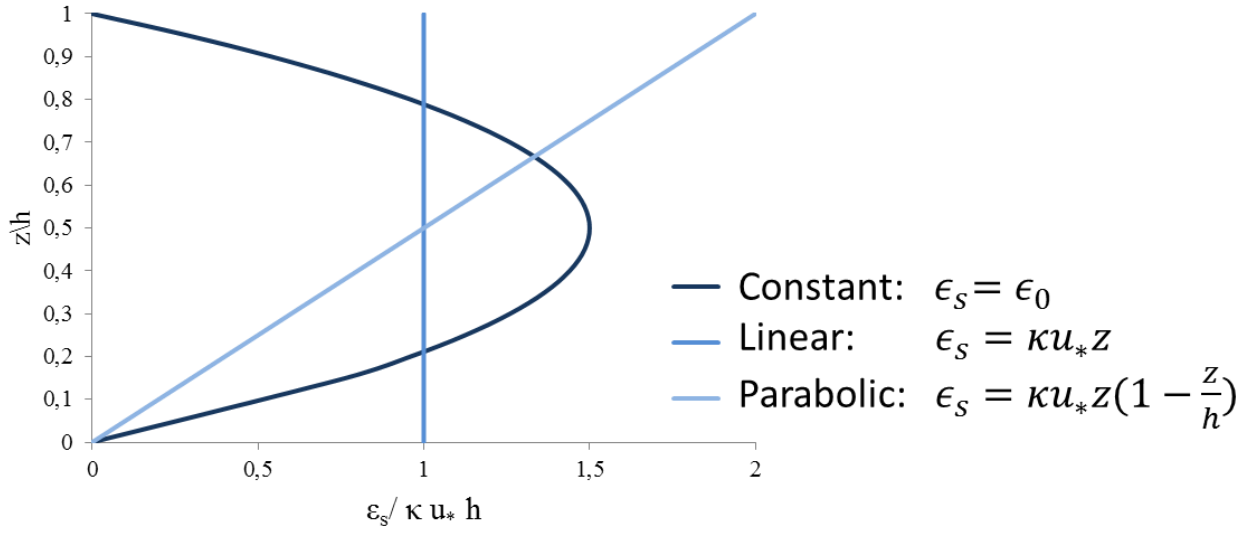


**Figure 12: Different shapes of eddy diffusivity profiles (Sistermans, 2002).**

The eddy diffusivity profile can also be described by a combination of these functions. Van Rijn (1984, 1993, 2007) developed different eddy diffusivity profiles for currents and waves (Figure 13). For steady currents the eddy diffusivity profile can be described by a parabolic-constant distribution (left graph in Figure 13). Concerning waves only, the vertical eddy diffusivity profile

can be described by a constant-linear-constant profile (right graph in figure 13). Combined waves and currents eddy diffusivity profiles can be derived by:

$$\epsilon_{combined} = \sqrt{\left(\epsilon_{s\,current}\right)^2 + \left(\epsilon_{s_{wave}}\right)^2} \qquad (2.15)$$

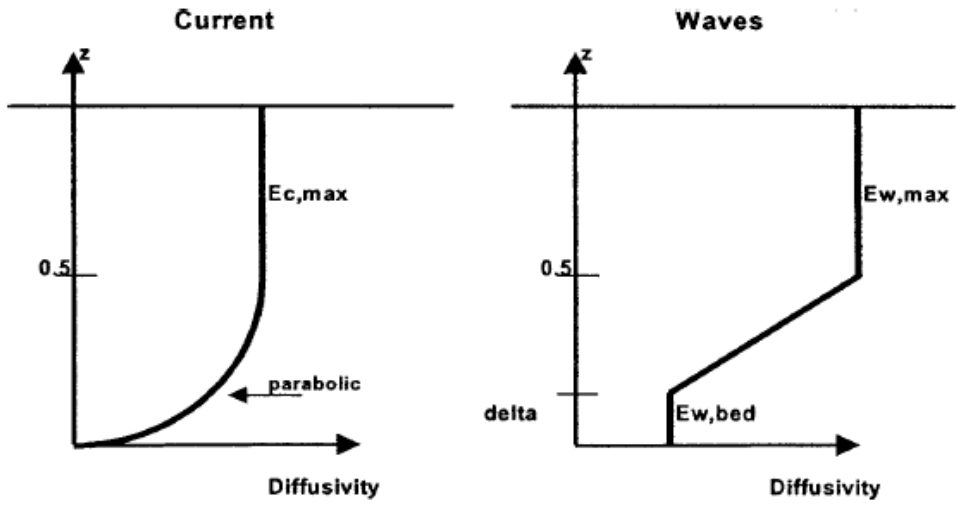


**Figure 13: vertical distribution of eddy diffusivity profiles after Van Rijn (2007).**

# 3 Methods

## 3.1 Study area

A four-week field experiment was conducted on the Dutch sandy coast 4 km southward from the village Egmond aan Zee (Figure 14) during October 2013. This area is widely used for studies on sand concentration, transport and other morphological studies. Egmond aan Zee is a practical study area by its accessibility and the presence of the ARGUS tower. The ARGUS tower monitors the area by taking time-exposure images (TIMEX) every 30 minutes during daylight. These TIMEX images are useful when determining wave breaking zones (Figure 15).


**Figure 14: Study area near Egmond aan zee, along the North Sea coast in the Netherlands. The coast is wave dominated and consists of 2-3 intertidal sandbars. Image from Google Earth (2014). The Measurement frame is the name of the frame with all measurement instruments.**

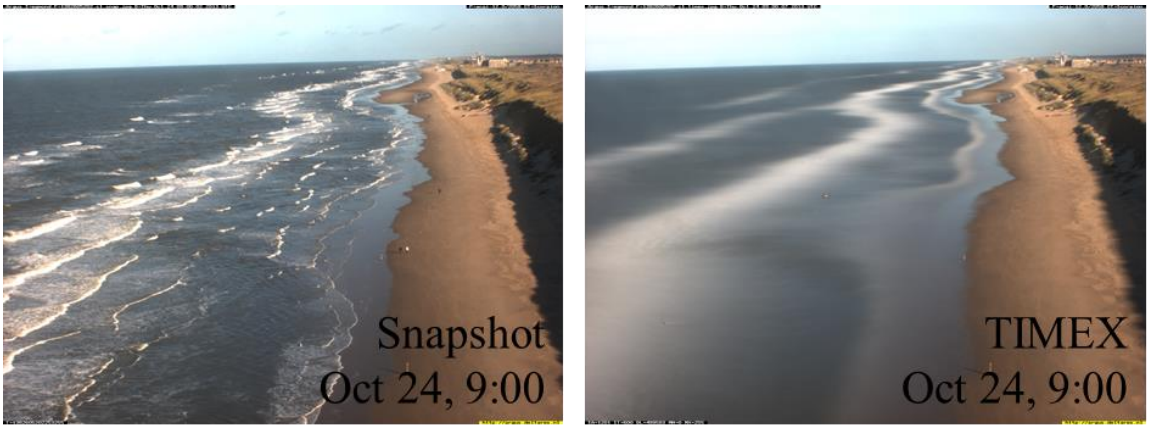


**Figure 15: Example snapshot and TIMEX image of the ARGUS tower at Egmond aan Zee. The TIMEX images represent a mean image and are useful to determine the wave breaking zone.**

The beach is bordered by dunes of 1-2 kilometers wide which suffer erosion during storms. In order to prevent erosion near the village Egmond aan Zee, sand nourishment takes place about every 10 years.

Since there is a wider range of weather conditions during autumn, the field campaign was planned for October. The beach is a wave dominated gently sloping beach, characterized by 2-3 intertidal sandbars separated by ~0.1 -1.0 m deep troughs. Breaking waves are most often spilling. The dominant wind and wave direction is South-West, but the highest waves originate from North West directions during storms. The tidal regime is semi-diurnal with a tidal range of 1.2 m during neap tide and 2.1 m during spring tide (Aagaard & Jensen, 2013). The tide is asymmetrical with a 4 hour rising tide and 8 hour falling tide (Price and Ruessink, 2008). The sand consists of well sorted sand, mainly quartz with a median grain size of 0.3 mm.

## 3.2 Instruments

The measurement frame was installed at a fixed location along the low water line in order to measure for the longest time as possible. The instruments used in this study are: two ElectroMagnetic Flowmeters (EMF) which measured cross-shore and longshore velocities, a pressure sensor, measuring wave characteristics and water depth and a sonar 3D ripple scanner, measuring ripple configuration for +/- 1$m^2$ each 15 minutes. Vertical SSC profiles were measured using 7 optical backscatter sensors (OBS), also called sand turbidity meters (STM). The bottom five STMs were part of a single device. On top of these, two separate STMs were placed higher in the water column (Figure 16). The Measurement frame also contained a float, starting measurements during submerged intervals and stopping measurements during emerged seawater intervals. All devices, except for the 3D ripple scanner, measured with a frequency of 4 Hz. Data was saved on a data logger and downloaded on a laptop twice a week at low tide.

The Measurement frame was positioned in line with the strongest longshore currents (NW) so the frame itself causes minimal disturbance. Although the frame was placed in a fixed position, instrument heights with respect to the seabed changed continuously due to morphological processes along the coast. Therefore, instrument heights were measured manually during low tide at daylight every day and adjusted when needed. The adjustments in measurement height were especially needed for the sand concentration measurements (STM). To measure vertical SSC profiles as good as possible, it is important to measure suspended sand concentrations close to the bed. If the distance between the lowest STM and the bed was larger than 10 cm, the lowest STM

was lowered to +/- 4 cm above the bed. Height adjustments of other instruments were only performed when these were buried in the sand. The development in instrument height is linearly interpolated between these measurements at low tide. During the daily measurements at low tide, sand samples were collected to determine grain size and fall velocity. The grain size and fall velocity were measured using a still water particle velocity tube and the method of Van Rijn (1993, eq. 2.4 and 2.5). Bed levels were measured with respect to the Dutch Ordnance level NAP using a DGPS. If large scale morphology changed drastically, DGPS surveys were driven with a quad.

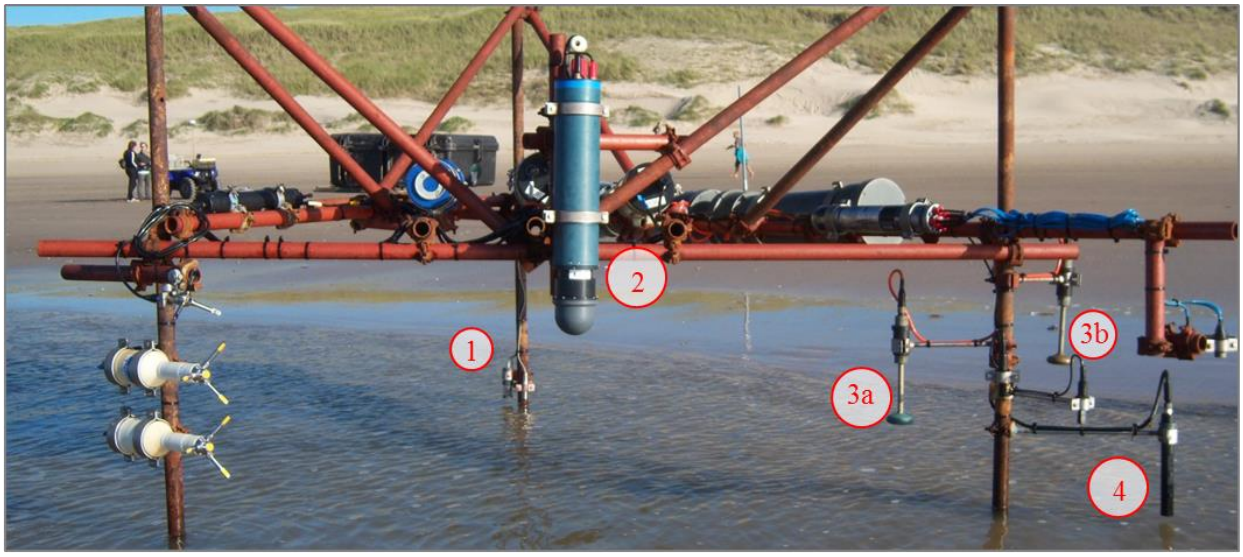


| # | Parameter | Instrument |
|---|---|---|
| 1 | Waveheight and waterdepth | Pressure sensor |
| 2 | Bottom morphology | 3D ripple scanner |
| 3 | Velocity | EMF |
| 4 | Sediment concentration | STM |

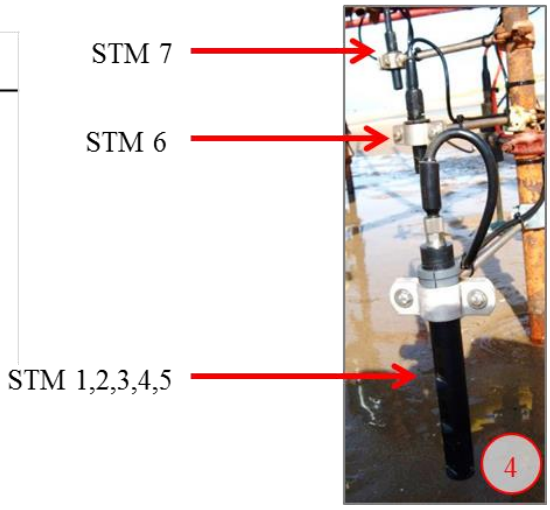


**Figure 16: Photograph of Measurement frame with measurement instrument 1-4. The STMs are positioned consecutively in the dominant direction of the strongest currents.**

## 3.3 Calibration data and pre-processing data

All measurements are expressed in millivolt. These values are converted to physical units by calibrating all instruments. Calibration numbers and curves are known from previous studies with the Measurement frame and are used in this study without any adjustments. The mean parameters are determined for every15 minutes as the focus of the study is on average vertical SSC profiles and the 3D ripple scanner creates scans for each 15 minutes. By choosing the same time interval, mean hydrodynamic parameters are easier to analyze in combination with bedform scans.

### *Water depth*

Water depth is derived from the pressure signals (instrument 6, Figure 16). Firstly, the signal is corrected by the barometric pressure signal measured by a separate pressure gauge located in the village Egmond aan zee. Since the pressure sensor measures the water depth above the pressure sensor, the total water depth can be calculated by adding the manually measured instrument height:

$$h = \frac{\overline{p_w}}{g\rho_w} + h_{sensor} \tag{3.1}$$

Where:

| | | | |
|---|---|---|---|
| $h$ | : | Water depth | $[m]$ |
| $h_{sensor}$ | : | Height pressure sensor | $[m]$ |
| $g$ | : | Gravitational acceleration | $[ms^{-2}]$ |
| $\rho_w$ | : | Sea water density | $[ms^{-2}]$ |
| $\overline{p_w}$ | : | Mean water pressure above the sensor corrected for pressure from local device | $[Pa]$ |

### *Wave height and velocity*

For every 15 minutes a wave energy spectra was computed using a Hamming window with a length of three minutes, 50% of overlap and 18 degrees of freedom. From these spectra a spectral moment was calculated with

$$H_{high} = 4\sqrt{m_0 HF} \tag{3.2}$$

$$H_{low} = 4\sqrt{m_0 LF} \tag{3.3}$$

Where:

| | | | |
|---|---|---|---|
| $H$ | : | Wave height | $[m]$ |
| $m_0$ | : | Zeroth moment of the wave energy spectra | $[m]$ |
| $HF$ | : | High frequency $0.05 < f < 1\ Hz$ | |
| $LF$ | : | Low frequency $0 < f < 0.05\ Hz$ | |

From linear wave theory, the maximum near-bottom orbital velocity ($U_{bw}$) and orbital excursion length ($d_0$) is calculated.

Mean cross-shore ($\bar{u}$) and longshore ($\bar{v}$) velocities are calculated for every 15 minutes. Only the upper EMF is used for the data analysis since the lowest EMF was sometimes burrowed in the sand.

### *Nondimensional shear stress*

The combined wave-current bottom shear stress is calculated by an iterative calculation following based on the model of Grant and Madsen (1986):

$$\frac{1}{4\sqrt{f_{cw}}} + log\frac{1}{4\sqrt{f_{cw}}} = \log\left(\frac{C_r u_b}{\omega z_0}\right) - 1.65 + 0.24\left(4\sqrt{f_{cw}}\right) \quad (3.4)$$

Where:

| | | | |
|---|---|---|---|
| $f_{cw}$ | : | Bottom friction factor for combined waves and currents | $[-]$ |
| $C_r$ | : | Factor describing relative ratio of wave and current skin friction | $[-]$ |
| $u_b$ | : | Maximum wave-induced bottom particle velocity | $[m/s]$ |
| $\omega$ | : | Radial frequency | $[rad/s]$ |
| $z_0$ | : | Dynamic bottom roughness length | $[m]$ |

With the iterative calculated bottom friction factor $f_{cw}$, the wave shear velocity can be calculated by: $u_{*_w} = \sqrt{0.5\ f_{cw} U_{bw}}$ . Where $U_{bw}$ is the maximum wave-induced bottom particle velocity from linear wave theory. Current shear velocity can be calculated by: $u_{*_c} = \sqrt{0.5\ f_{cw} U_{bc}}$ .

Where $U_{bc}$ is the current speed at the top of the wave current boundary layer ($\delta_{cw}$), which can be derived using a logarithmic law. The height of the wave-current boundary layer is calculated by: $\delta_{cw} = \frac{2\kappa u_{*w}\sqrt{C_r}}{\omega}$. The combined shear velocity is calculated through: $u_{*cw} = \sqrt{C_r}\, u_{*w}$.

The non-dimensional shear stress for waves only, currents only and combined waves and currents is given by the Shields parameter, calculated with:

$$\theta = \frac{u_*^2}{(\rho_s - \rho_w) g D_{50}} \tag{3.5}$$

### *Bedforms*

Data from the sonar 3D ripple scanner were processed and analyzed by Schrijvershof (2014). Bed states were determined visually, inspired by the classification of Dumas et al (2005). The bedforms were classified in four categories: small-scale 2D ripples, small;-scale 3D ripples, large-scale bedforms and super-positioned small-scale ripples on large-scale bedforms (Figure 17). Small-scale 2D ripples are identified by ripple crests and troughs abreast with several successions in an image (Figure 17.a). Small-scale 3D ripples are similar to 2D ripples but ripple crests and troughs merge into each other and are spread out irregularly over the seabed (Figure 17.b). When bedforms were scanned partly, they were classified as large-scale bedforms (Figure 17.c). Sometimes, small-scale ripples could develop on top of large-scale bedforms. These bedforms were classiefied as super-positioned ripples. Ripple classification, length and height processed by Schrijvershof (2014) are used in this study without any adjustments.

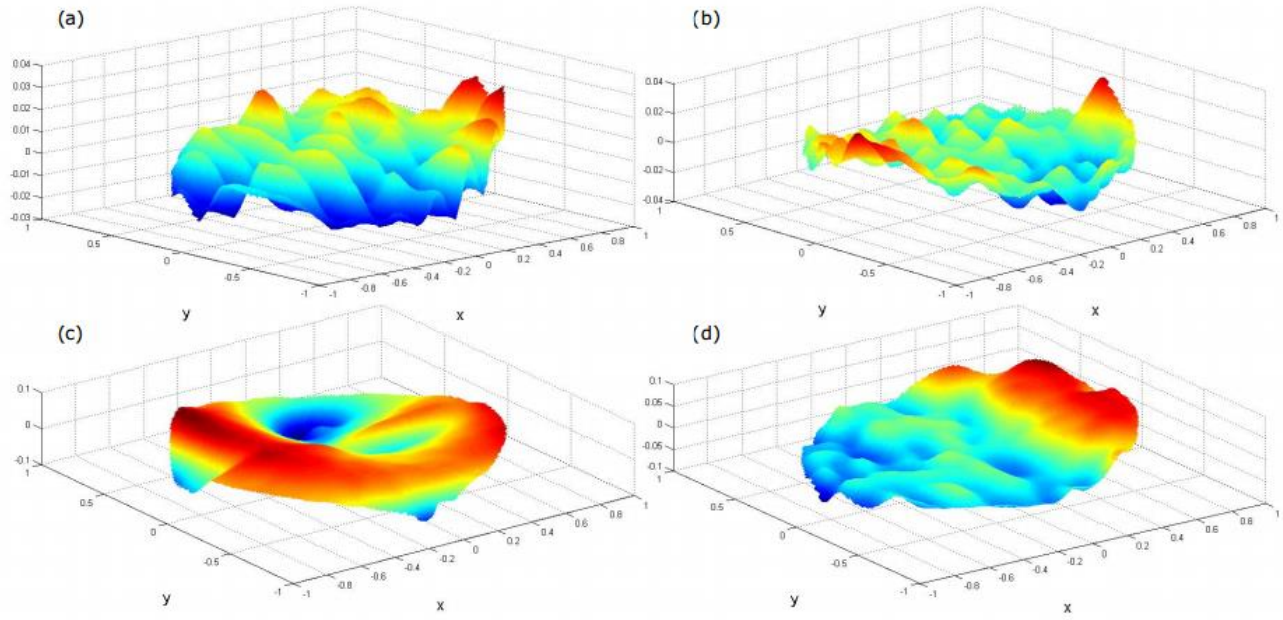


**Figure 17: Examples of different classified bedform states after Schrijvershof (2014); a: small-scale 2D ripples, b: small-scale 3D ripples, c: large-scale bedforms, d: super positioned small-scale bedforms on a large-scale bedform.**

### *Suspended sand concentration*

Figure 18.a shows calibrated suspended sand concentration signals for all seven STMs. However, the signal does not return to zero but to a value of about 1.5 $g/l$. This is due to inaccuracies in calibration at low concentrations. It can be corrected by subtracting a certain percentile of the calibrated signal. In figure 18.b, four corrections are applied with the different percentiles 0, 0.5, 1 and 5. It can be seen in figure 18.b that the choice of the percentile has no influence on the shape of the vertical SSC profiles. The choice of percentiles only shifts suspended sand concentration in magnitude. In this study a correction with percentile 0.5 is chosen.

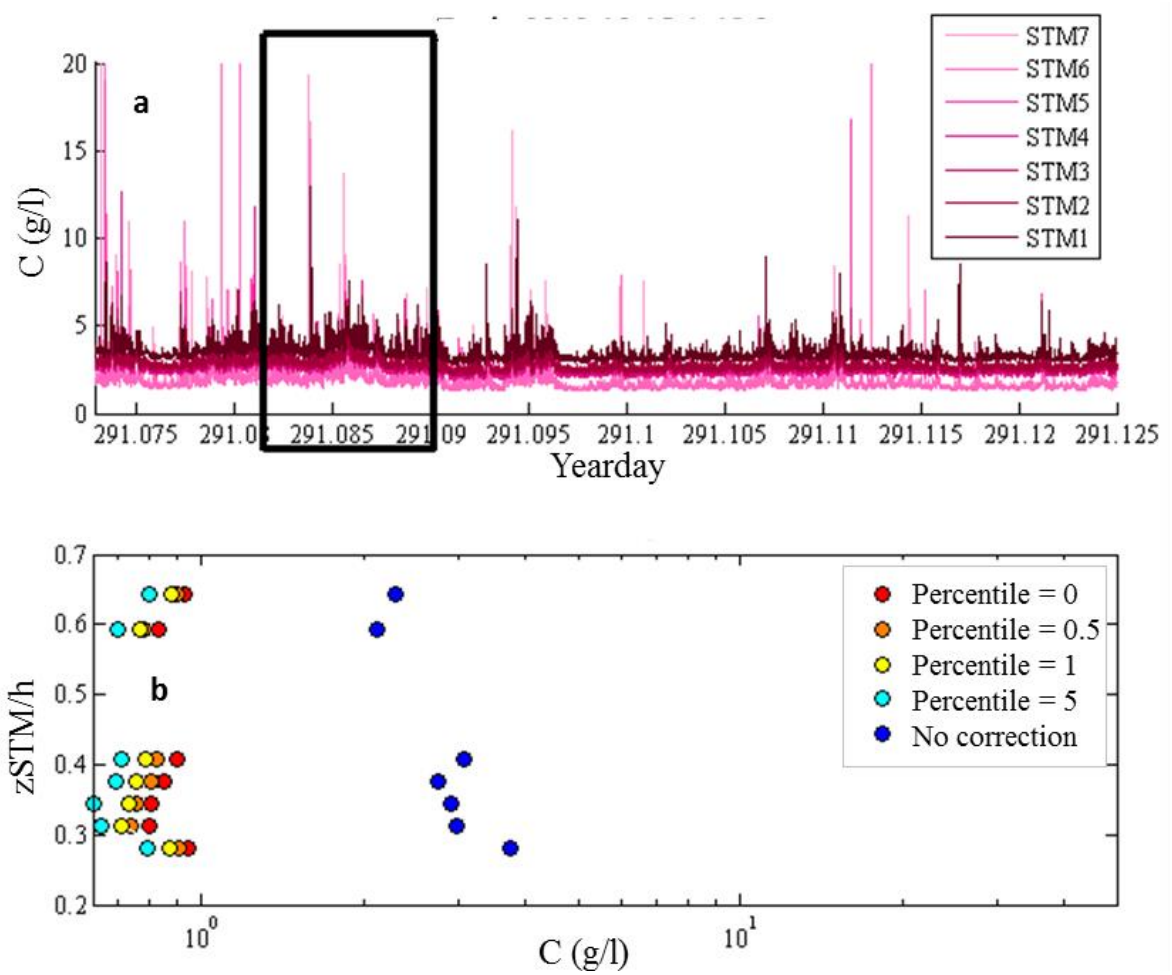


**Figure 18: A: Raw suspended sand concentration signal. B:Mean vertical SSC profiles with different percentile corrections.**

## 3.4 Data selection

Not all data could be used. Suspended sand concentration becomes overrated by, for example foam bubbles or seaweed. This overrated data should be filtered out before starting with data analysis. This selection is executed on the raw STM data measured. For suspended sand concentration near Egmond aan Zee, the rule of thumb is that concentration ranges between 0 – 50 $g/l$, with some spikes up to 100 $g/l$. The red frame in figure 19.a shows the interval of realistic suspended sand concentration at first sight. However, if looked at more detail (Figure 19.b), it can be seen that only half of the data is usable within the red frame. STM 7 (the upper STM) still show high concentration peaks within the red frame because of foam bubbles. In this way, a visual distinction is made between usable and unusable data for each tidal cycle.

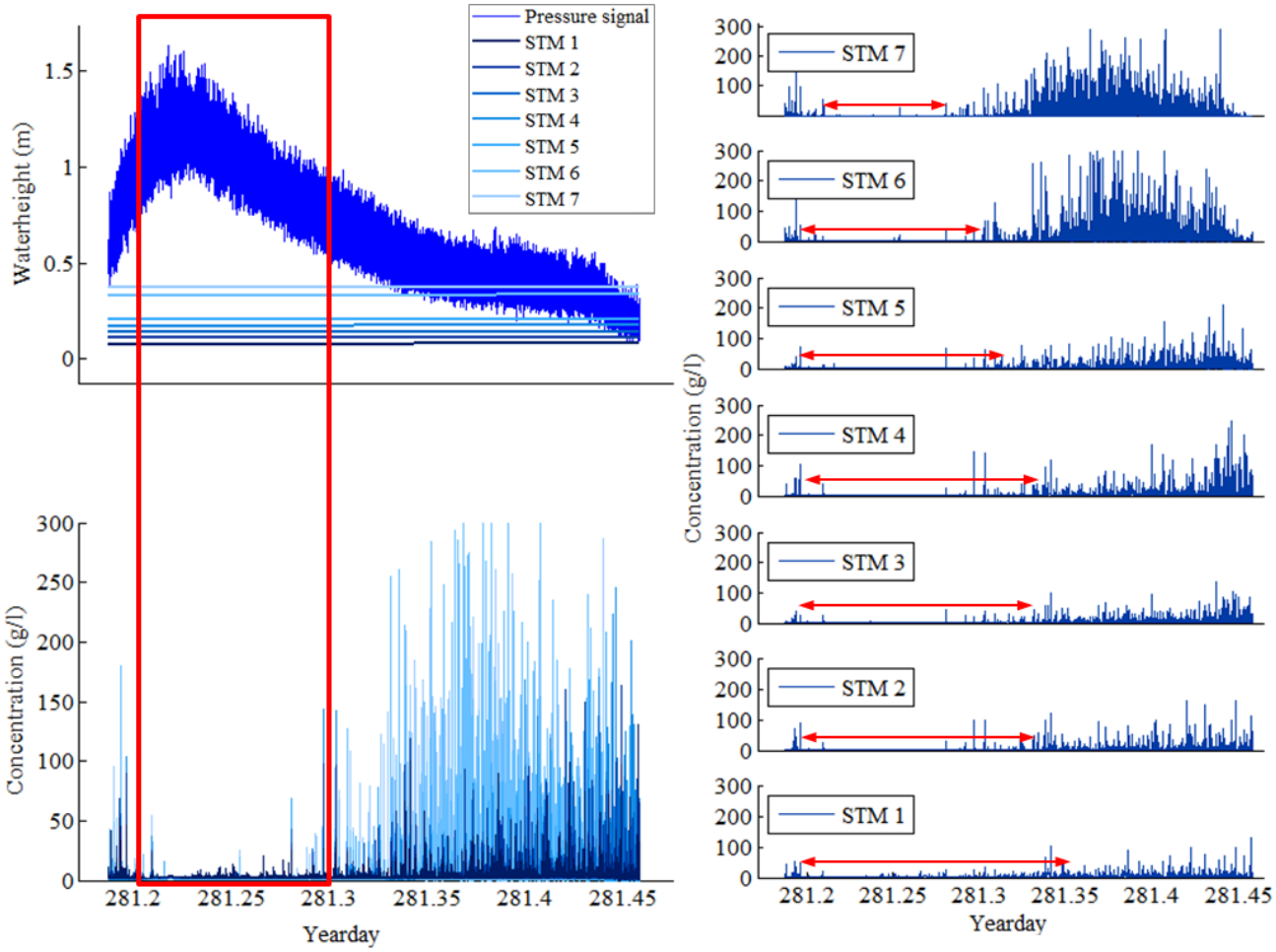


**Figure 19: A1: Water depth signal measured in 4 Hz. The horizontal lines show the STM height for all 7 STMs. A2: Raw STM signal for all 7 STMs. B: Detailed raw STM signals for all STMs separately.**

However, low suspended sand concentration is not automatically usable. Foam bubbles might disrupt the measurements, but it appears that sand concentration is measured because of low values. Foam bubble disturbance can be seen in the raw data signal when the highest sand concentration is measured at STM7 followed by decreasing peaks in ‘concentration’ by lower STMs (c.f. purple arrows in figure 20). Physically this would mean that sand entrainment starts at the top of the water column. This can only happen if sand originates from the upper water column. In reality, the source of the sand is down at the seabed, so these reversed peak signals are not usable due to foam bubbles. This visual filtering by following the signal peaks is also applied to each tidal cycle.

It turned out that disturbances by foam bubbles similar as shown in figure 20 mostly occurred during higher energetic conditions e.g. storms or when wave broke around the measurement frame. Of the total 3937 15 minute bursts, only 188 quarter are useful. From which approximately half was caused by rising and filling water and about and the other half by foam bubbles due to higher energetic conditions.

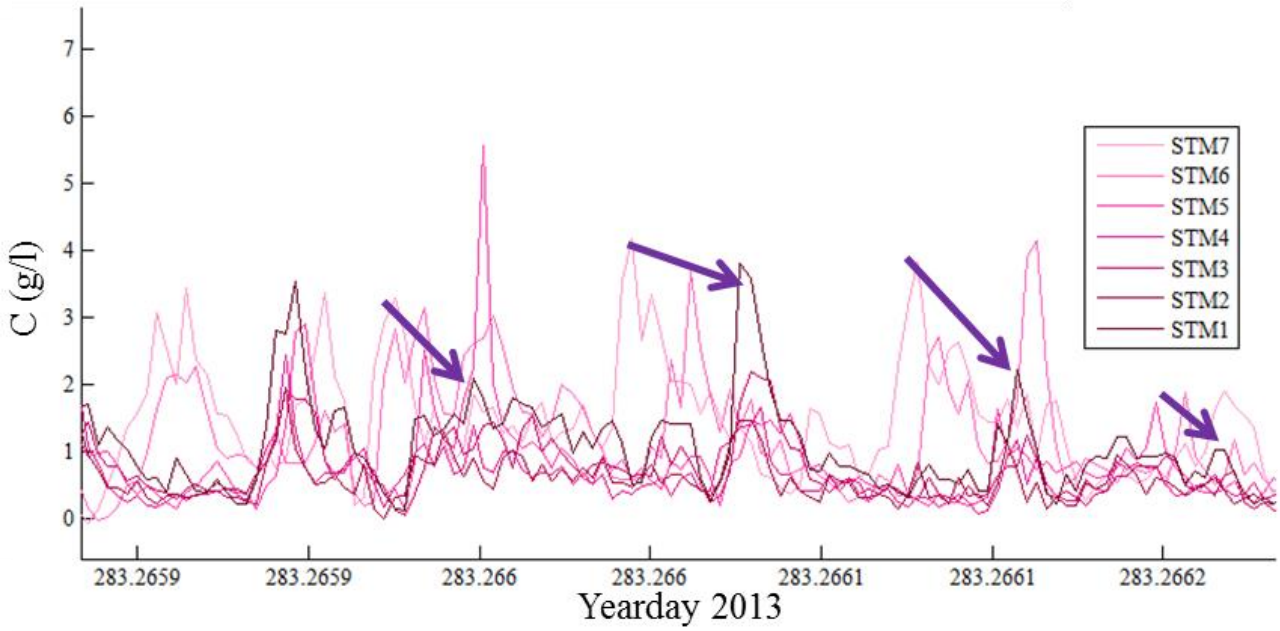


**Figure 20: Unusable suspended sand concentration signals since highest peaks are measured by the upper STM (STM7) followed by decreasing peaks measured by lower STMs.**

## 3.5 Reference concentration and eddy diffusivity calculations

Reference concentrations are calculated by extrapolating an exponential curve through each mean sand concentration profile to the reference height after Van Rijn (1993) $z_{ref} = 2 * D_{sand}$ (Figure 21). An exponential curve is used since the solution of the diffusion equation is exponential (eq. 2.2). Eddy diffusivities are calculated in two ways: analytically and by using the first order linear ordinary differential solution. The analytical method can be described by:

$$\epsilon_s = w_s \bar{c} \frac{dz}{d\bar{c}} \tag{3.6}$$

The first order linear ordinary differential method used can be described by:

$$\epsilon_s = w_s z / \log\left(\frac{C(z)}{C_0}\right) \tag{3.7}$$

Where $C_0$ is the extrapolated reference concentration using the exponential fit.

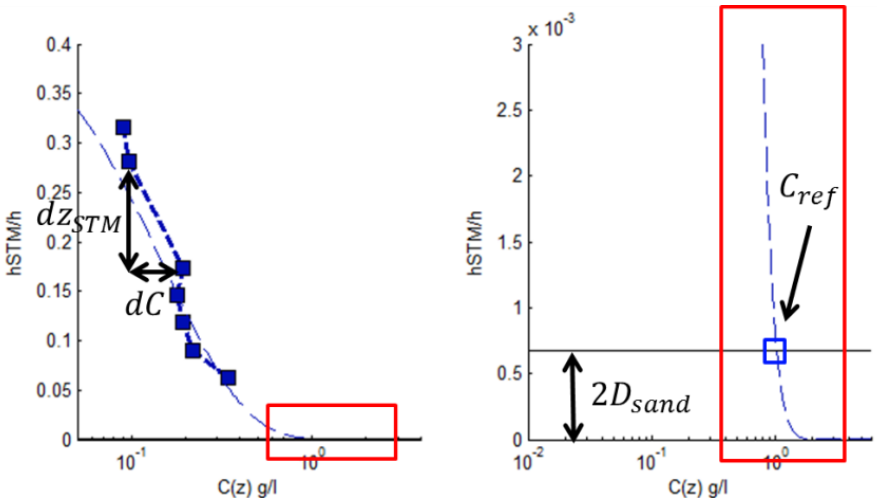


**Figure 21: Reference concentration is derived from an extrapolation of an exponentially fitted curve.**

# 4 Results

## 4.1 Hydrodynamics and morphological change in the field campaign

The weather conditions varied from calm to more energetic during the field campaign in October 2013. Highest offshore waves occurred during the first storm from 10 to 12 October. This storm is followed by three smaller storms (Figure 22.a). The offshore water depth ranged from maximal +1.5 m NAP during flood and minimal -1 m NAP during ebb tide (Figure 22.b).

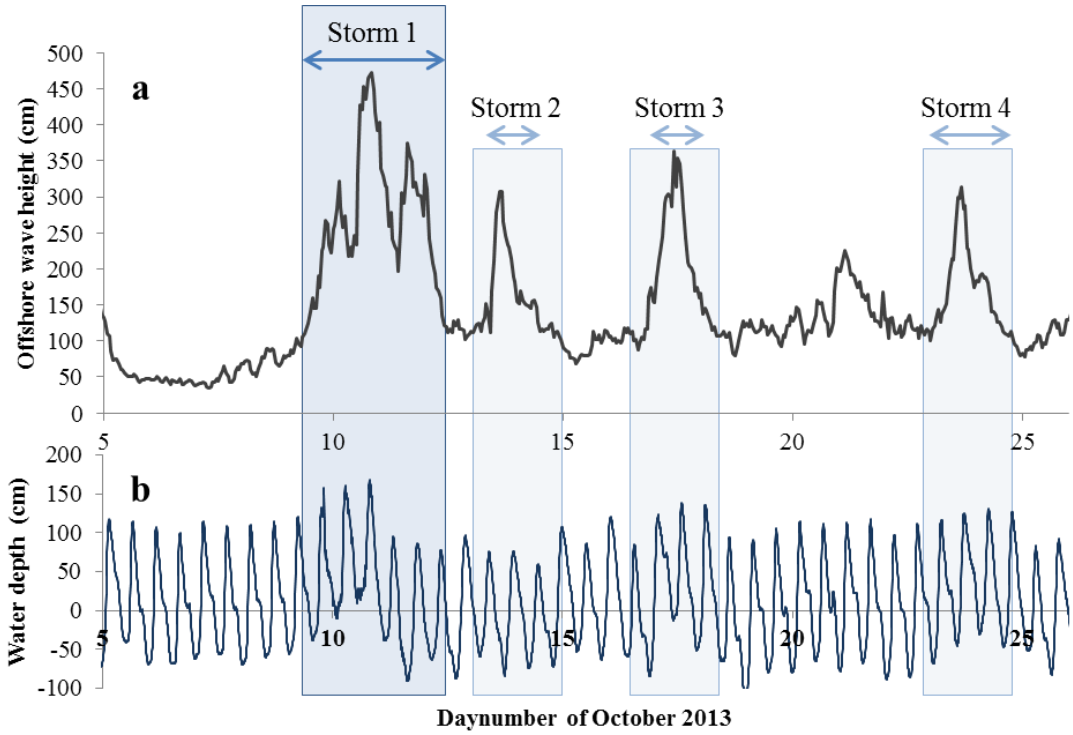


**Figure 22: Offshore significant wave height measured at IJmuiden munitions dump (live.waterbase.nl, 2015).**

An overview of 15-minute burst averaged hydrodynamic conditions near the measurement frame and concentrations measured are shown in figure 23. Selected data (following the method described in section 3.4) are indicated with blue dots. Short wave heights ranged between 0.1 – 1m and are strongly modulated by the tide: at relatively high water depths, higher short waves could develop and similarly, low waves developed with low water depths. This is typical for surf zone bores. Infragravity waves varied between 0.03 m and 0.12 m. Cross shore mean current velocities were relatively constant at -0.15-0.09 m/s, while selected longshore mean currents peaked at ~0.7 m/s when the waves approached the coast obliquely (Figure 23.c). These peaks lead to relatively high values for the current Shields parameter $\theta_{current}$ to 0.3. The wave Shields

parameter can be correlated to the short wave heights. From this figure 23.d, it becomes clear that the conditions were wave dominant since the wave Shields parameter is predominantly higher than the current Shields parameter. Selected mean sand concentrations were highest with 5 g/l around 20 October, but fluctuated mainly between 0-2 g/l (Figure 23.e).

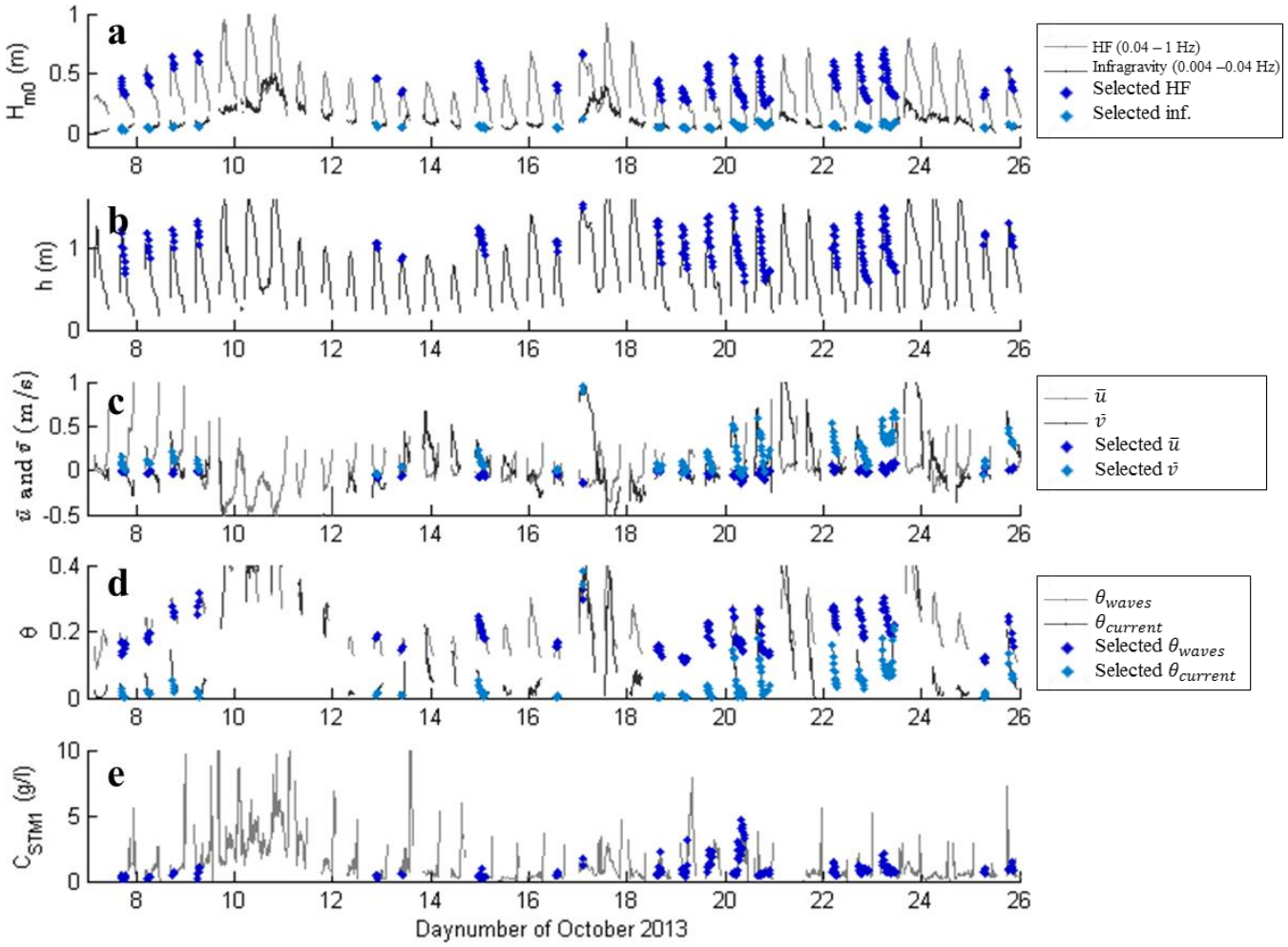


**Figure 23: Overview of mean wave heights, water depth, cross- and longshore current during the field campaign in Egmond aan Zee, October 2013. The black and grey lines show the measured data during the field campaign. The blue dots indicate the data selection. With figure A showing: Wave height and infragravity wave height. B: Water depth. C: Mean longshore and cross shore velocity. D: Suspended sand concentration.**

During the field campaign, the orientation of the measurement frame relative to the sandbar changed from the crest of the sandbar (Figure 24.a) to the landward side of the sandbar (Figure 24.b). A local depression under the frame arose (Figure 24.c). At the end of the field campaign, the sandbar was connected to the beach (Figure 24.d). Between these states, the morphology changed subtly in bed level and distance from the troughs between sandbar and beach. These

small changes in morphology result in different locations of the wave breaking zone with respect to the Measurement frame. Environmental conditions changed not only because of varying hydrodynamic conditions, but also through instrument relocation with respect to the sandbar and wave breaking zones. The shifting in morphology is also reflected in the cross sections derived by the DGPS surveys (Figure 25). On 12 October, the measurement frame was on top of a sandbar. At the end of the field campaign (October 25$^{th}$ ) the sandbar grew up on the beach: no trough can be seen between sandbar and beach.

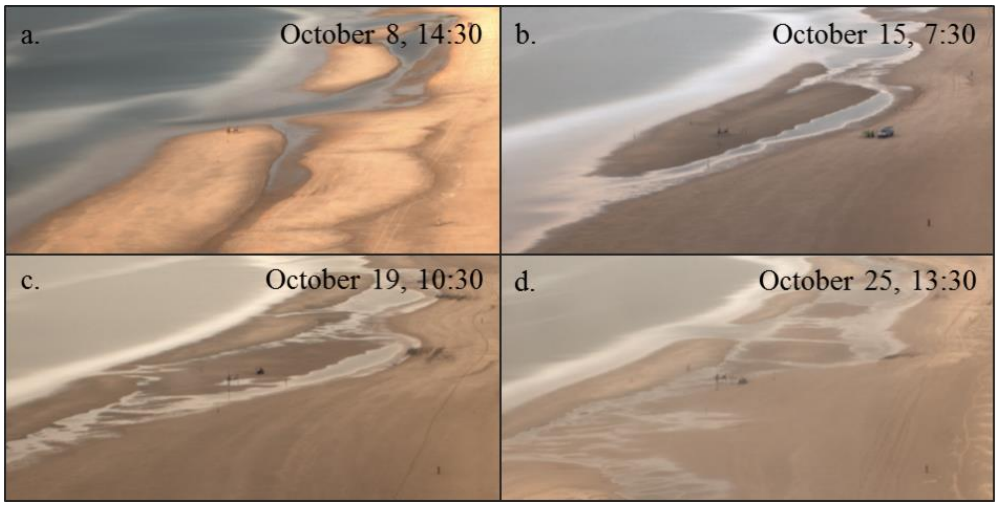


**Figure 24: The orientation of the measurement frame with respect to the sandbar during the field work campaign. A: The frame is on top of a sandbar. B: The sandbar is shifted northward, making the frame's orientation on the landward side of the sandbar. C. The frame is positioned in a local depression. D. The sandbar is connected to the beach. Pictures are taken by the ARGUS tower at Egmond aan Zee.**

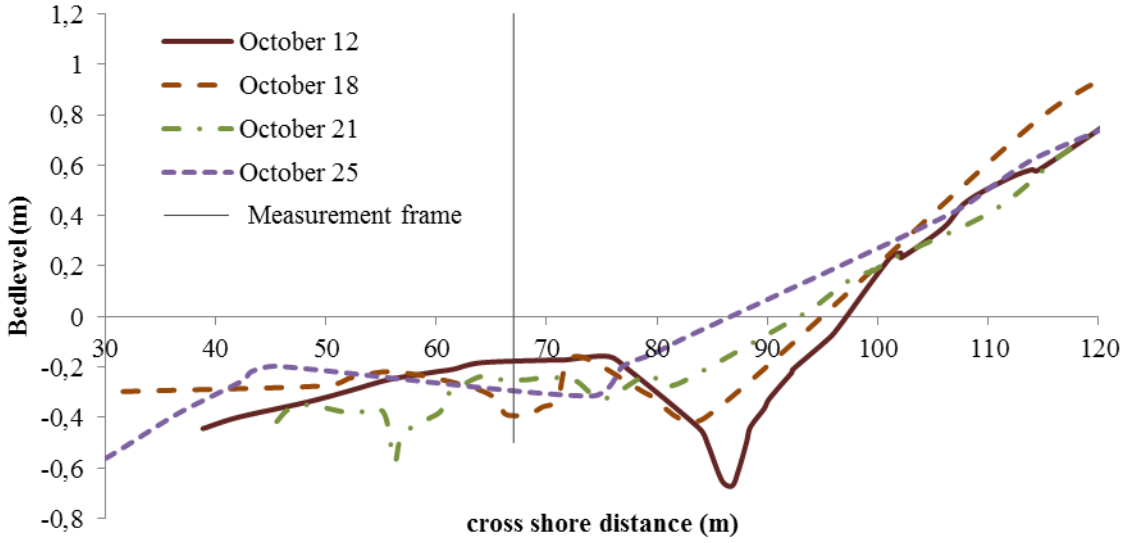


**Figure 25: Changes in beach profile showing a decreasing trough depth between sandbar and beach. On 12 October the frame is positioned on top of the sandbar. On 18 October a local depression surrounds the frame. On 21 and 25 October the sandbar is sanded on the beach.**

## 4.2 Controlling hydrodynamic parameters on sand concentration

In practice, Shields parameters are used as an indication of the environmental energetic conditions. It is to be expected that high Shields numbers correspond to high sand concentrations since high and breaking waves induce more turbulence which can move more sand compared to low waves and weak longshore currents. However, in figure 26 this can not be seen. In this figure, three vertical SSC profiles are plotted for different environmental conditions: calm, intermediate and rough. On the calmest day (Figure 26.a), significant wave height and Shields parameters show the lowest values. The most energetic conditions experience largest significant wave heights and Shields parameter (Figure 26.c). On this rough day at October 23, highest sand concentrations were measured. While the lowest sand concentrations were measured on the intermediate day (October 22). Sand concentrations at different Shields numbers has been analyzed on multiple days and leads to the conclusion that low Shields parameters do not automatically imply low suspended sand concentrations.

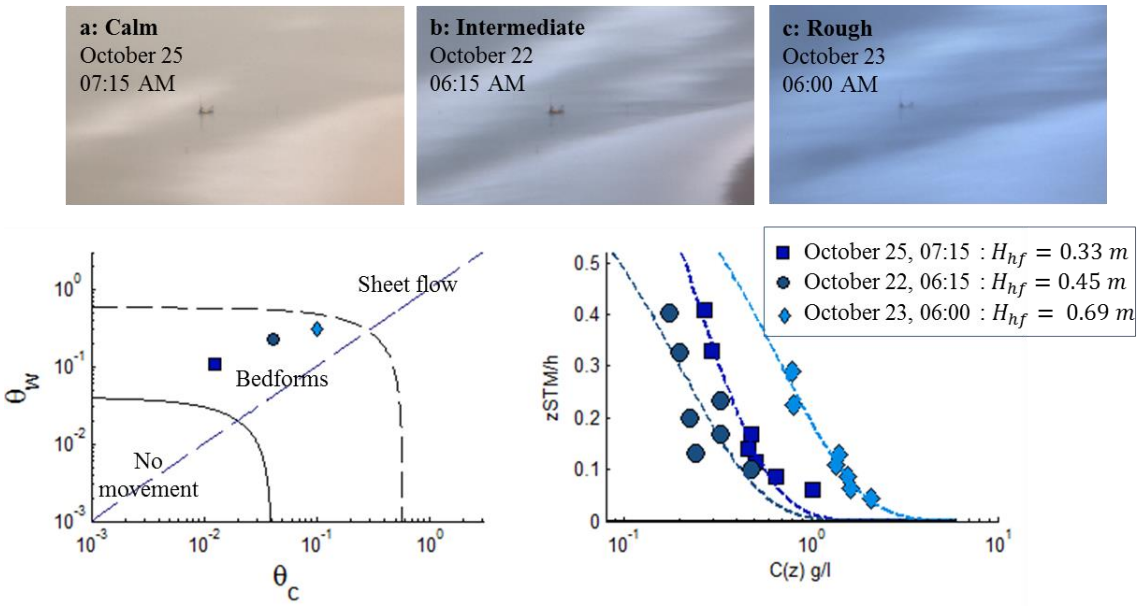


**Figure 26: Rough weather conditions do not imply higher sand concentrations. Sand concentration is lowest on 22 October, the day with the highest Shields parameter and wave height values. Sand concentration is highest on October 25th .**

The absence of a trend between hydrodynamic parameters and suspended sand concentration is also shown in figure 27. For all wave heights, sand concentration ranges between $0 - 1.5\ g/l$, no clear trend can be found. The color indicates STM heights above the bed in order to show that differences in STM heights, which is maximal 10 cm, do not control the missing trend. For

example at $z_{STM} = 0.15\ m$ above the seabed (yellow dots in figure 27), the sand concentration is quite stable around $0.25\ g/l$ while wave heights ranges between $0.35 - 0.6\ m$. Also for mean longshore velocities, no clear trend can be found between sand concentration and the hydrodynamic parameter. Sand concentration peaks around $\bar{v} = 0\ m/s$ and also at $\bar{v} = 0.35\ m/s$. Figure 27 shows that hydrodynamic parameter values alone do not provide sufficient information to understand which conditions ensure high sand concentrations. From literature it is known that ripples and morphology are significant in sand entrainment. The next paragraph describes the measured ripples in the surfzone and corresponding sand concentration during October 2013.

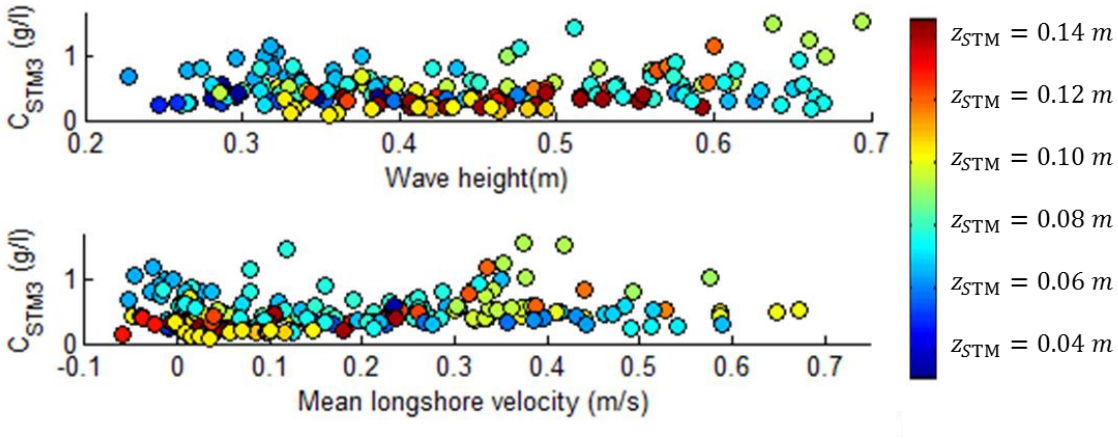


**Figure 27: Sand concentration plotted against hydrodynamic parameters. The color of the circles indicate the value of the STM height above the bed. No clear trend can be found between sand concentration and wave height and longshore velocity.**

## 4.3 Ripple influence on suspended sand concentration

The classified ripples are placed in the Shields diagram introduced in the literature review (Figure 28). With increasing $\theta_c$ ripple types shift from small-scale 2D tot small-scale 3D to large-scale ripples. Super-positioned ripples are a class apart since these ripples are formed from the transition from large-scale to small-scale ripples. The occurrences of super-positioned ripples are within the hydrodynamic range of small-scale 3D ripples. However, these small-scale ripples are formed on top of relict large-scale ripples which are developed during more energetic conditions (blue circle, Figure 28). Although there is a shift in ripple type with increasing $\theta_c$, ripple types are not normative for specific hydrodynamic conditions. The occurrences overlap between different ripple types. Especially small-scale 3D ripples (yellow diamonds, Figure 28) range over all hydrodynamic conditions measured during the field campaign.

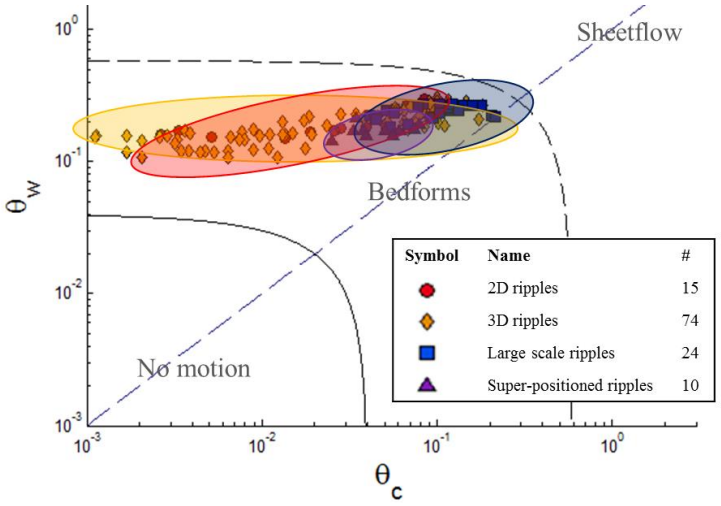


**Figure 28: Shield stability diagram with occurences of ripple type. With increasing $\theta_c$ ripples shift from small-scale 2D to small-scale 3D to Large-scale ripples.**

To investigate the influence of different ripple types on vertical SSC profiles, mean vertical SSC profiles are plotted for each ripple type in figure 29 d-f. Without any division between environmental conditions, based on the current Shields parameter, vertical SSC profiles for small-scale 2D and 3D ripples are less steep compared to large-scale and super-positioned ripples (Figure 29.d). The distinction in steepness is caused in the lower part of the water column: the near-bed concentrations for large-scale ripples are lower compared to near-bed concentration for small-scale ripples. From $z_{STM}/h = 0.2$, vertical SSC profiles show the same steepness and quantity (Figure 26.d). However, these differences in steepness between small and large-scale ripples become less clear when a distinction is made between the current Shields parameter. In Figure 29.e, vertical SSC profiles for all ripple types show similar courses. This division is based on the range of occurrence of large-scale ripples. When $\theta_c$ is larger than the minimal $\theta_c$ measured ($\theta_c = 10^{-1.3} \sim 0.04$) at large-scale ripples, vertical SSC profiles are plotted in figure 29.e. Vertical SSC profiles measured at lower values for the current Shields parameter are plotted in figure 29.f. From this division it seems that the difference in steepness is more controlled by the environmental conditions, especially the current Shields parameter $\theta_c$ which relate to longshore velocities, than the ripple type. The vertical SSC profile for small-scale 2D and 3D ripples for the lowest $\theta_c$ are less steep (Figure 29.f) compared to the vertical SSC profiles for the higher $\theta_c$ values (Figure 29.e). This is mainly caused by the higher near-bed concentrations for the vertical SSC profiles at lower Shields parameter. However the error bars indicate overlap between all

vertical SSC profiles which indicates that there is no specific vertical SSC profile per ripple type nor environmental condition.

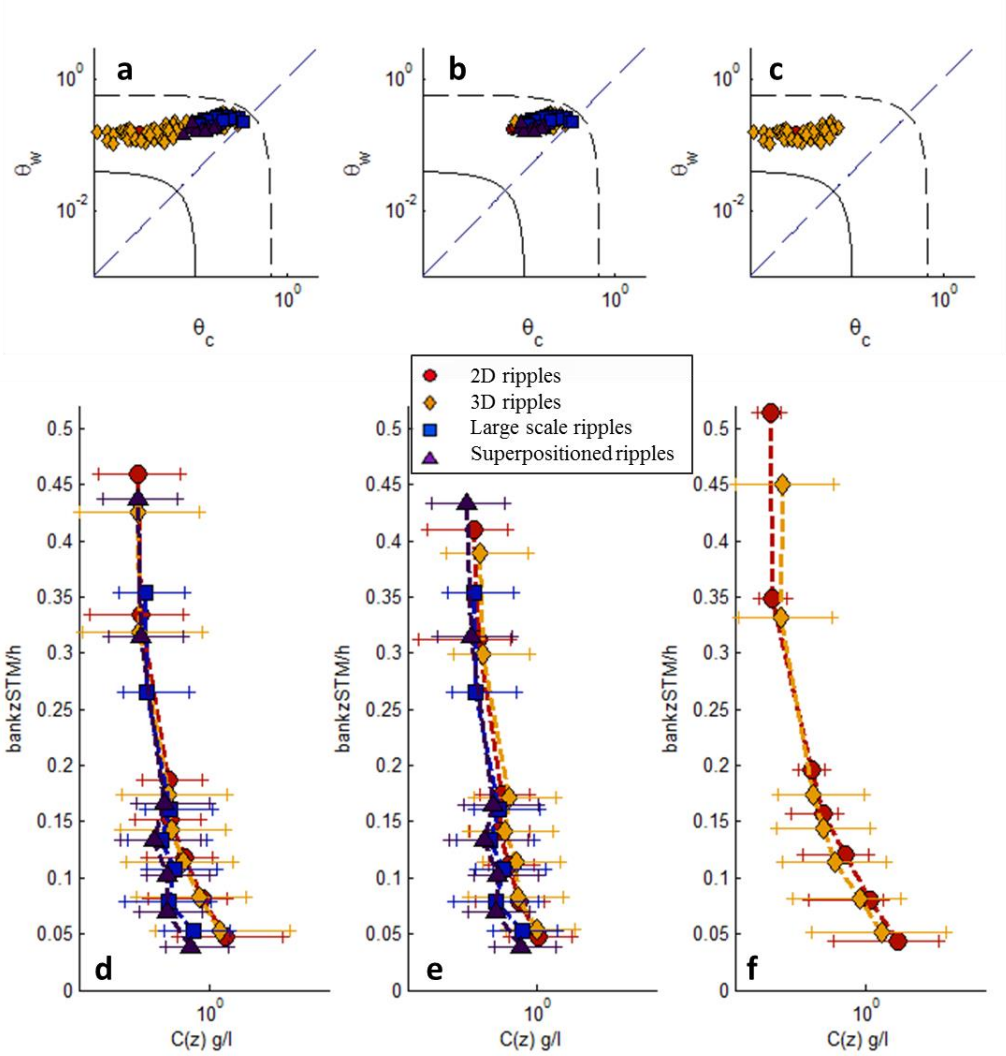


**Figure 29.a-c: Shields diagram indicating environmental conditions per ripple type; d: Mean vertical SSC profiles for all current Shields parameters; e: Mean vertical SSC profiles for the highest current Shields parameters; f: Mean vertical SSC profiles for the lowest current Shields parameters.**

## 4.4 Eddy diffusivity

From section 4.2 it appears that there is no direct relation between hydrodynamics and suspended sand concentration. In section 4.3, although the distinction between environmental conditions based on $\theta_c$, no clear difference can be seen between vertical SSC profiles and different ripple types. This lack of relations is also visible in figure 30. In this figure the analytically solved eddy diffusivity (see methods section 3.5) is plotted against the relative STM height above the bed. Figure 30.a shows the eddy diffusivity profiles for different environmental conditions, expressed

in $\theta_{cw}$, indicated with colored dots. Figure 30.b shows eddy diffusivity profiles per classified ripple type. To compare these eddy diffusivities with relations from literature, three different models are also plotted in the figure.

For both environmental conditions and ripple type, the eddy diffusivity values scatter over all classes and no distinction can be made between eddy diffusivity profile shapes. For example the eddy diffusivity for large-scale ripples (blue squares, Figure 30.b) ranges within the band of all derived values. This makes it impossible to specify one type of eddy diffusivity profile for large-scale ripples alone which form a distinction from other ripple types.

In general the analytically calculated eddy diffusivity is higher compared to eddy diffusivities calculated with formulas from literature. This means that the measured sand concentration profiles are steeper compared to other studies where the formulas are based on. This can be true since these sand concentration profiles are measured in the surfzone where waves break causing more turbulence. Therefore sand concentration profiles are steeper compared to deep water concentration profiles.

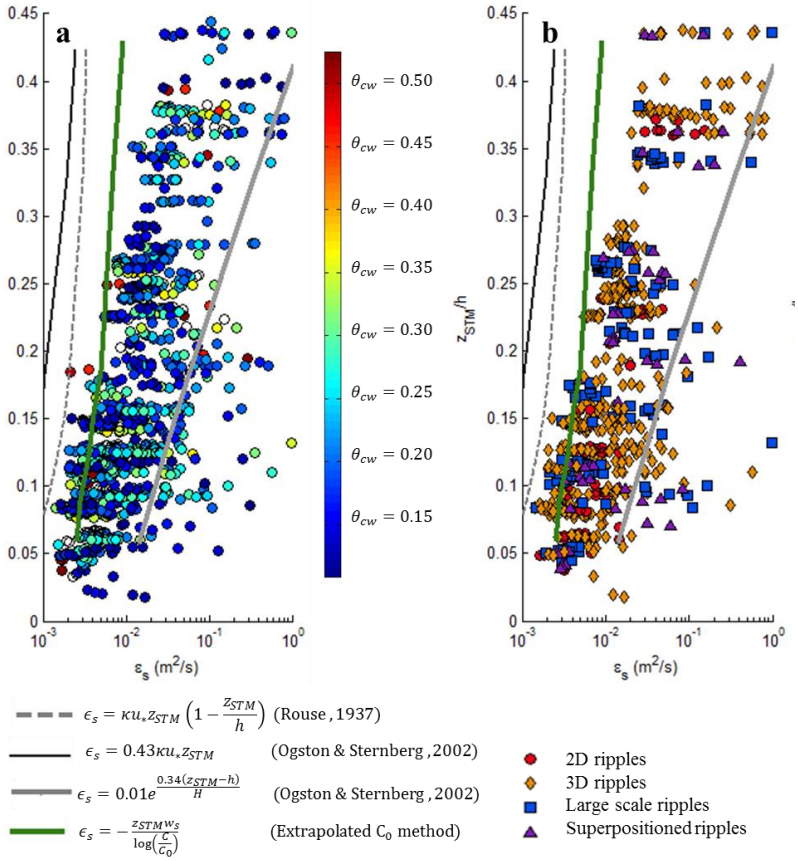


**Figure 30: Eddy diffusivity profiles for all observations. A: The color of the dots indicates the combined Shields parameter $\theta_c$. B: The symbols indicate different ripple types.**

## 4.5 Reference concentration

From previous sections it can be concluded that the shape of vertical SSC profiles cannot easily be allocated to hydrodynamic parameters or ripple types. The magnitude of the suspended sand concentration is predominantly determined by the bottom concentration. In this section two predictors from Nielsen (1986, 1992) are tested with reference concentrations from field measurements.

The extrapolated reference concentration is plotted against the combined Shields parameter per classified ripple type (Figure 31).In this scatter plot, no trend can be seen for small-scale 2D and 3D ripples range. Reference concentrations for small-scale ripples range between $\sim 0.5 - 10\ g/l$ for all combined Shields parameter values. This reach shows a flatter trend than the trend described by $C_0 = 0.10\rho_s\theta_{cw}^3$. This implies that reference concentrations for small-scale ripples were less dependent on the shields parameter compared to model studies described by both formulas.

Reference concentrations for large-scale ripples increase slightly with increasing combined Shields parameter (blue squares, Figure 31). Although the values are less compared to the model described by $C_0 = 0.10\rho_s\theta_{cw}^3$, they show a similar steepness as this model. However, the reference concentrations for large-scale ripples show a similar trend to the model, the values are not unique for large-scale ripples only. Small-scale 3D ripples have comparable values for higher Shields parameters (Figure 31).

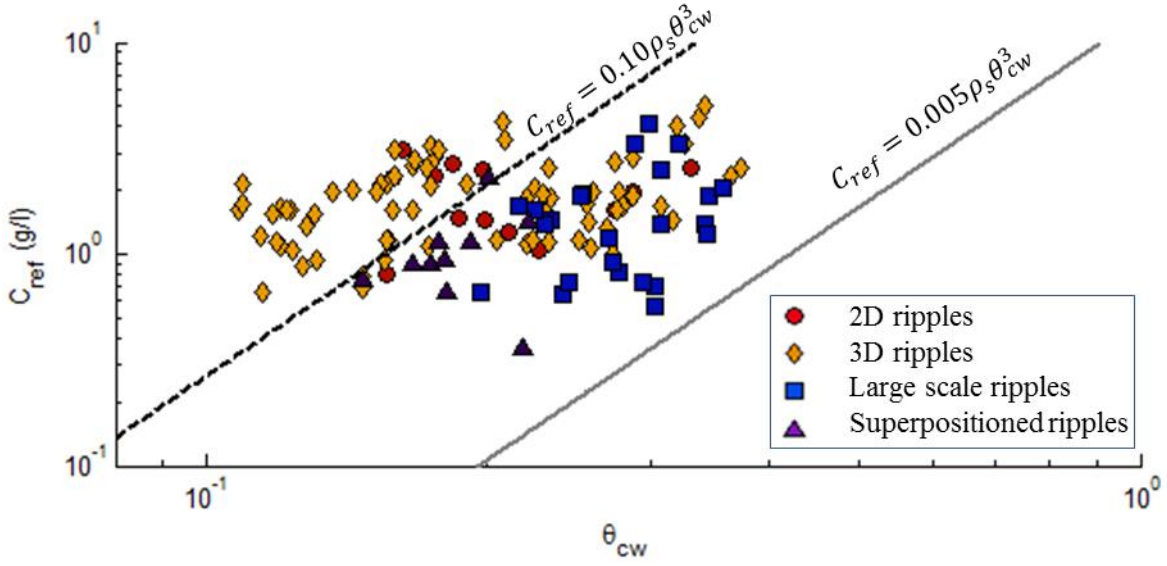


**Figure 31: Reference concentration per ripple type against combined Shields parameter.**

The similarities for all environmental conditions and ripple types are also shown in the vertical SSC profiles plotted in figure 32: all vertical SSC profiles have resembling shapes confirming similar values for all reference concentrations. When a distinction is made between high and low energetic conditions, vertical SSC profiles for relatively high energetic conditions ($\theta_c > 0.04$) are steeper compared to vertical SSC profiles at lower Shields parameters. This distinction is also visible for the reference concentrations. The relative high energetic conditions fit well with the model, but the low energetic conditions have much higher reference concentrations compared to the model (Figure 32). This makes that there seems to be a relation between hydrodynamic conditions (expressed in Shields parameters) and vertical SSC profiles in terms of shape and reference concentrations. However the differences in characteristics are minimal and can not be allocated to one specific parameter.

## 4.6 Suspended sand concentration per tide cycle

Many tidal cycles show just one ripple type while hydrodynamic conditions changed during that tidal cycle. This is partly because the ripple type depends on relict configurations of the bedforms besides prevailing hydrodynamic conditions. Depending on the strength of the hydrodynamic conditions during high tide, ripple type can change. However, these changes do not respond instantaneously to the hydrodynamic conditions and experience delays in its formation. This is also called hysteresis. This results, as with hydrodynamic parameters (Figure 27), that ripple type only is not sufficient to understand which conditions ensure high sand concentrations. A certain ripple type ensures not just one possible sand concentration. With any ripple type, multiple sand concentrations are possible.

### *Two different suspension mechanisms*

By analyzing sand concentrations for each tide cycle, two ‘suspension mechanisms’ arise:

1. Sand concentration peaks at falling water (Figure 32.a).
2. Sand concentration peaks at high tide (Figure 32.b).

This classification between suspension mechanism 1 and 2 is shown in figure 32 by the red and black dots on top of the bed level line. For example, all tidal cycles from 8-10 October show suspension mechanism 1. Generally, suspension mechanism 1 occurs for small-scale 3D ripples, except the first tidal cycle on 20 October. Suspension mechanism 2 appears for all ripple types.

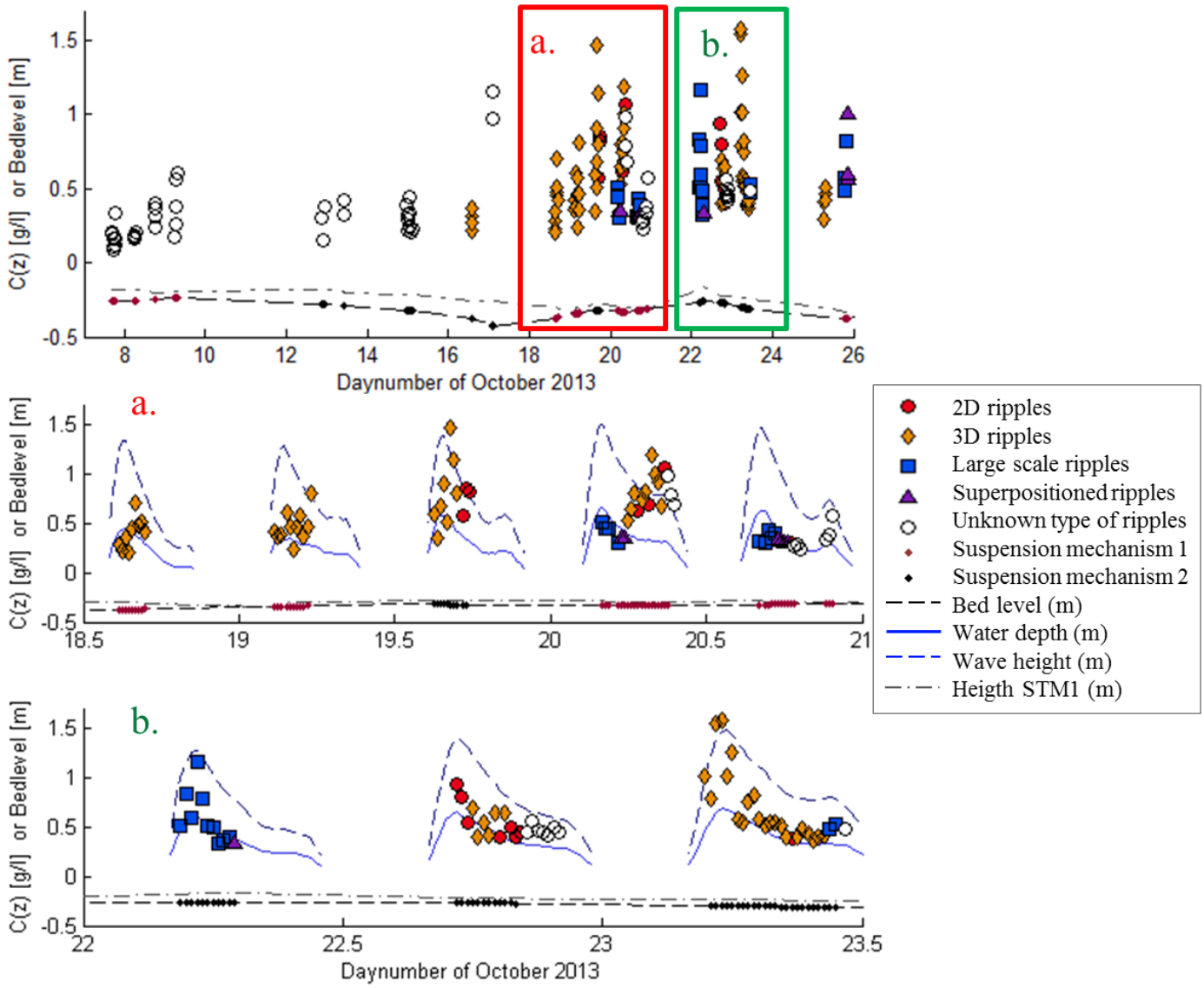


**Figure 32: Sand concentration during the field campaign indicated by symbols for different ripple types. Two suspension mechanisms can be found. Fram a: suspended sand concentration peaks at falling water. Fram b: suspended sand concentration peaks at high tide.**

When the occurrences of suspension mechanism 1 and 2 are plotted in a Shields diagram (Figure 33), the same distinction in environmental conditions arise as shown in the vertical SSC profiles (Figure 29) and reference concentrations (Figure 31). Suspension mechanism 1 occurs over the entire range of Shields numbers and suspension mechanism 2 only appears in the higher energetic conditions ($\theta_c > 10^{-1.55} \sim 0.028$).

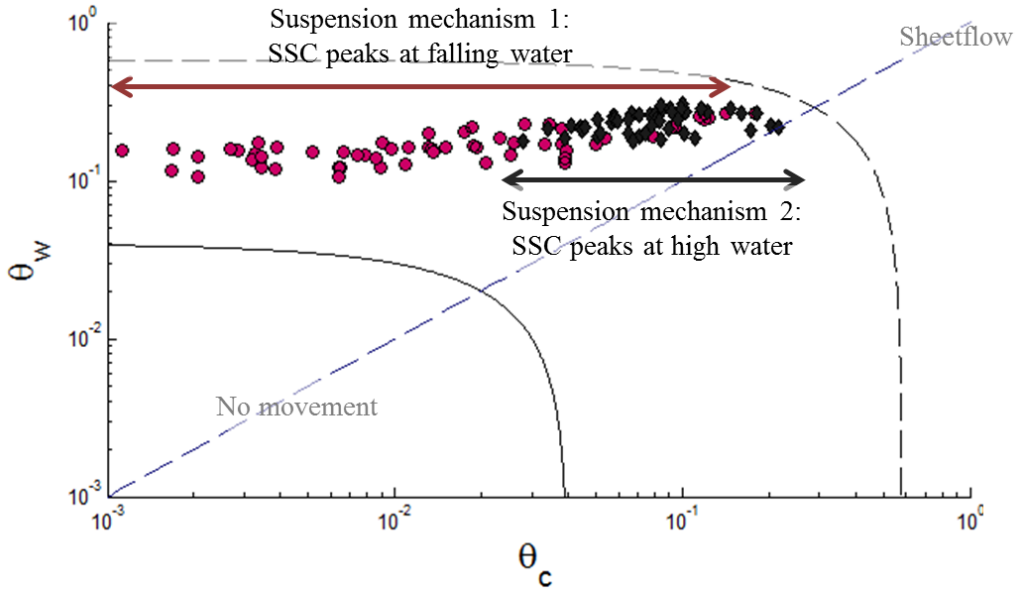


**Figure 33: Division of suspension mechanism 1 (red dots) and suspension mechanism 2 (black diamons) in a Shields diagram. Suspension mechanism 2 only occurs at higher energetic conditions.**

To zoom further into the different suspension mechanisms and associated suspended sand concentration, figure 34 and 35 show examples of the different suspension mechanisms during one tidal cycle. The bedforms during both days consisted of 3D ripples only. The relative wave height indicates the amount of breaking waves. The higher the relative wave height, the more waves are broken. Peaks in suspended sand concentration correlate with higher relative wave heights and more breaking waves in the surrounding which are visible by the white bands imaged by the ARGUS tower (indicated by red frameworks in figure 34 and 35). Further visual analysis shows similar patterns on other days: sand concentrations are highest when most waves break in the surroundings and with higher relative wave height values.

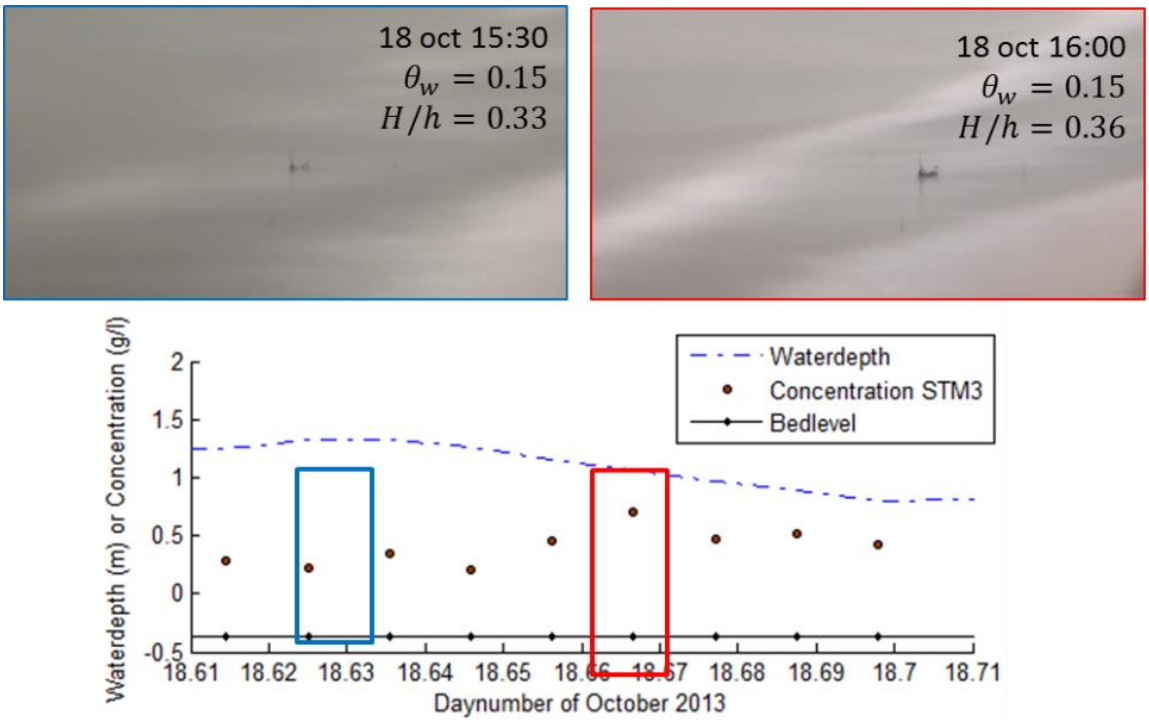


**Figure 34: Example of suspension mechanism 1: suspended sand concentration peaks at falling water. The ripple type was 3D ripples throughout the tidal cycle. Blue framework: during high tide, the suspended sand concentration is relatively low. Red framework: suspended sand concentration peaks.**

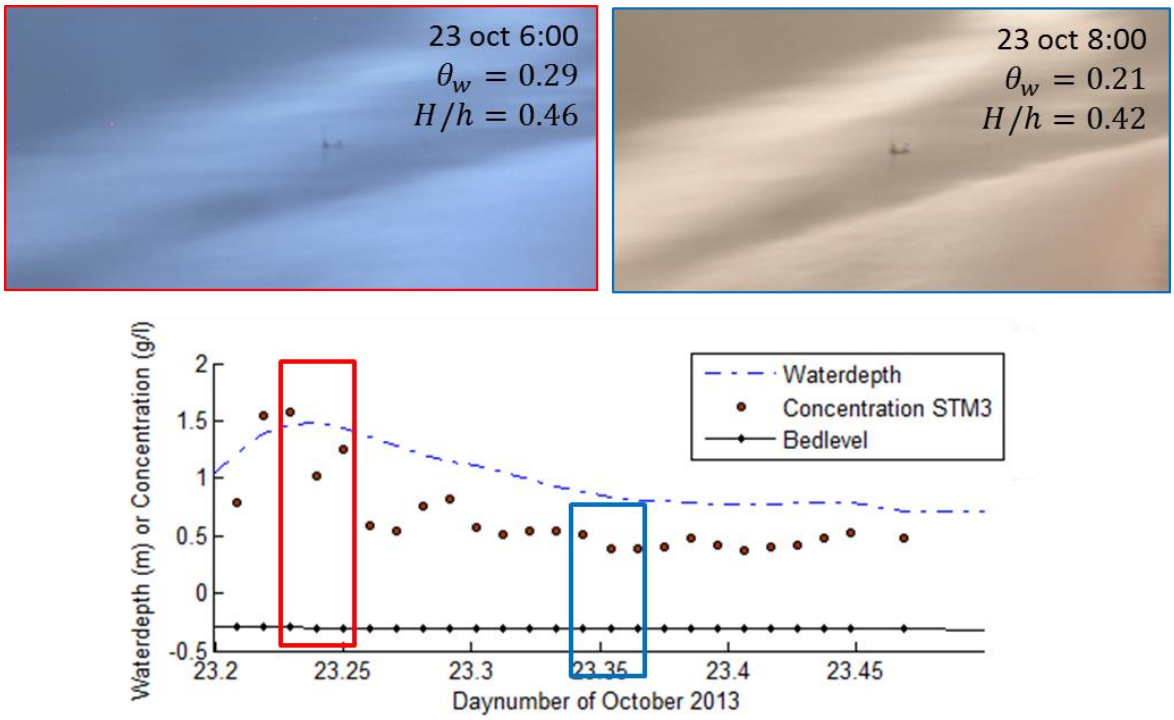


**Figure 35: Example of suspension mechanism 2: suspended sand concentration peaks at high tide. The ripple type was 3D ripples throughout the tidal cycle. Red framework: during high tide, the suspended sand concentration peaks. Blue framework: suspended sand is relatively low.**

The relation between suspended sand and the relative wave height is plotted in figure 36. Highest sand concentrations are reached when the relative wave height ranges between $0.35 < H/h < 0.5$., which are breaking waves. Suspension mechanism 2 only occurs between this range with high sand concentrations, while suspension mechanism 1 varies over all measured values ranging from $0.27 < H/h < 0.6$. However, within the range of $0.35 < H/h < 0.5$ both low and high concentrations occur for the same relative wave number. For example at $H/h = \sim 0.46$, both sand concentrations appear around 0.1 $g/l$ and 1.5 $g/l$ . In this figure It is again visible that sand concentration can not linearly be related to the Shields wave number since for both low (dark blue circles at $0.26 < H/h < 0.35$) and high values (red circles at $0.5 < H/h < 0.6$) lead to relatively low sand concentrations with a maximum around 0.5 $g/l$.

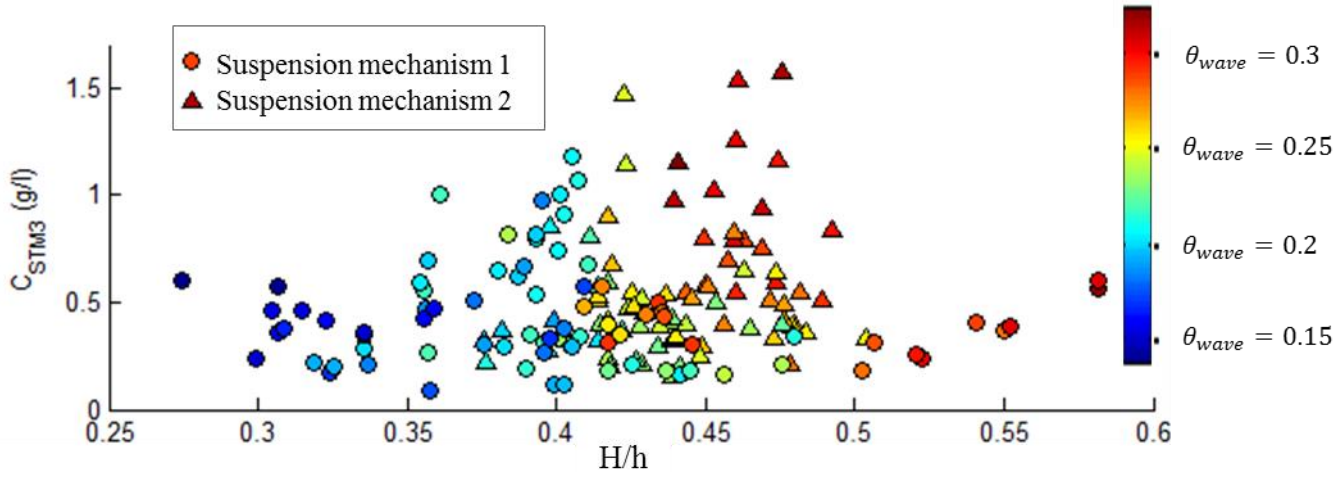


**Figure 36: Sand concentration plotted against relative wave height $H/h$ for suspension mechanism 1 (circles) and suspension mechanism 2 (triangles). The color indicates the wave Shields parameter.**

# 5 Discussion

Summarizing, the results tell that vertical SSC profiles cannot be predicted on the basis of hydrodynamics or ripple type only. It is related to the combination between ripple type and orientation of waves with respect to its breaking point, indicated with the relative wave height. However, the relative wave height gives an indication only and due to the varying morphology it is difficult to compare the values with each other. For example: during high waves and high setup conditions, relative wave heights of 0.5 can occur. This is also possible with relatively low waves and therefore low setup conditions, the ratio between low wave heights $H$ and low water depths $h$ can still give 0.5. These examples are essentially two different conditions with different vertical SSC profiles.

The influence of different conditions has also be found and studied by e.g. Ogsten & Sternberg (2002) and Aagaard & Jensen (2013). Aagaard end Jensen found characteristic vertical SSC profiles depending on wave type and therefore orientation of the waves with respect to its break point. For breaking waves in the outer surfzone (S) and surf bores in the inner surfzone (SB), vertical SSC profiles are Rouse shaped (Figure 37). For waves in the middle of the breaking zone (BZ), vertical SSC profiles are exponential shaped (linear on a log-linear plot in figure 37). These different shape of profiles also provide different eddy diffusivity profiles. Wave in the breaking zone has a constant eddy diffusivity, waves outside have parabolic or linear shaped eddy diffusivity profiles (Aagaard & Jensen, 2013). This classification is similar to found vertical SSC profiles in this study. Generally the shape was similar to the inner surfzone (SB) and became steeper with increasing Shields number which is characteristic for the breaker zone (Figure 29). Although this was not clearly reflected in eddy diffusivity profiles since they all had similar values.

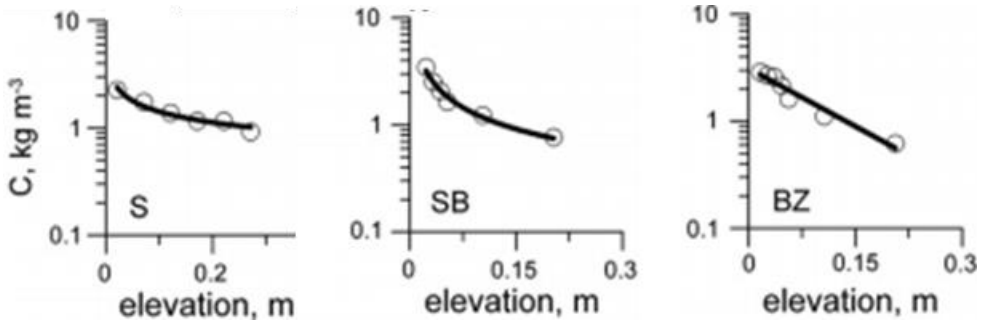


**Figure 37: Examples of mean sand concentration profiles recorded at Egmond aan Zee by Aagaard and Jensen (2013). For breaking waves in the surfzone (S) and surf bores in the inner surfzone (SB), concentration profiles are Rouse-shaped. Sand concentration in the breaker zone (BZ) is exponential. N.B. the turned axes, elevation is on the x-axis and sand concentration is on the y-axis.**

## 5.1 Reference concentration

The extrapolated reference concentrations in this study are a factor of 10 higher compared to other field measurements (e.g. Green & Black, 1999; Dolphin & Vincent, 2009, Figure 38). However, water depth was much shallower during this study in Egmond aan Zee. This could be an explanation for the higher extrapolated values, since higher bed roughness in shallow water can generate higher bed concentrations (Van Rijn, 1993). This shallow water depth can also be the reason of the flat trend in reference concentration. Due to stronger wave impacts and bedform processes in depth between 1-3 m compared to 7 m depths, other processes than hydrodynamics play a significant role in near-bed concentrations. The difference in environmental conditions is also described by (e.g. Lee et al., 2004; Jayaratne & Shibayama, 2007; Aagaard & Jensen, 2013). They divided the environment in: broken or unbroken waves. For each environment, different reference descriptions exist. This is also visible in the study by Green and Black (1999, Figure 38), two different functions correspond to different water depths. Lee et al. (2004) also concluded that there is no formula to be used for all environments. For convenience, often the most easily understandable formula is used.

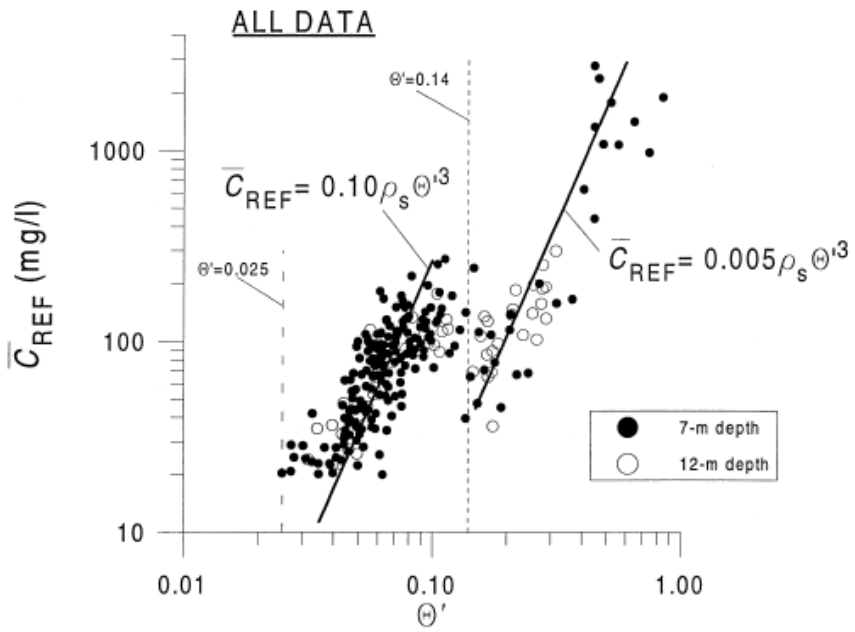


**Figure 38: Scatter plot of the reference concentration against the Shields parameter. All data is sorted by water depth (after Green and Black, 1999).**

Effects of bedforms was not reflected in figure 31 where all reference concentration range between the same values. This may be caused by the calculation of the reference concentration

using the simple extrapolation method. The calculation of the reference concentration by extrapolating may be incorrect since the reference height is standard set on $z_{ref} = 2 * D_{50}$. While in literature different reference heights are described depending on bedform heights. These factors are not included in the calculation of the reference concentration and therefore maybe not visible in figure 31. Possibly, reference concentrations are calculated too simply in this study eliminating the effects of the Shields parameter. This could be solved by using different reference heights for different bedform types. In this study, this is not further investigated since the focus of this study is on the steepness of the vertical SSC profile. The reference concentration forms the precondition and do not determined the steepness of the vertical SSC profile. Next section describes the results of the eddy diffusivity, the parameter which influence the steepness of the vertical SSC profile.

## 5.2 Eddy diffusivity

Eddy diffusivities of the field campaign dot not math to model studies plotted in figure 30. While, the these values have the same order of magnitude compared to other studies (e.g. Van Rijn, 1993; Ogsten & Sternberg, 2002; Thorne et al., 2009). An overview of different eddy diffusivity profiles is given in figure 39. It shows that many eddy diffusivity calculations exist. Still there is no clear formula found for the best eddy diffusivity calculation (Van Rijn, 1993), not even after 1993.

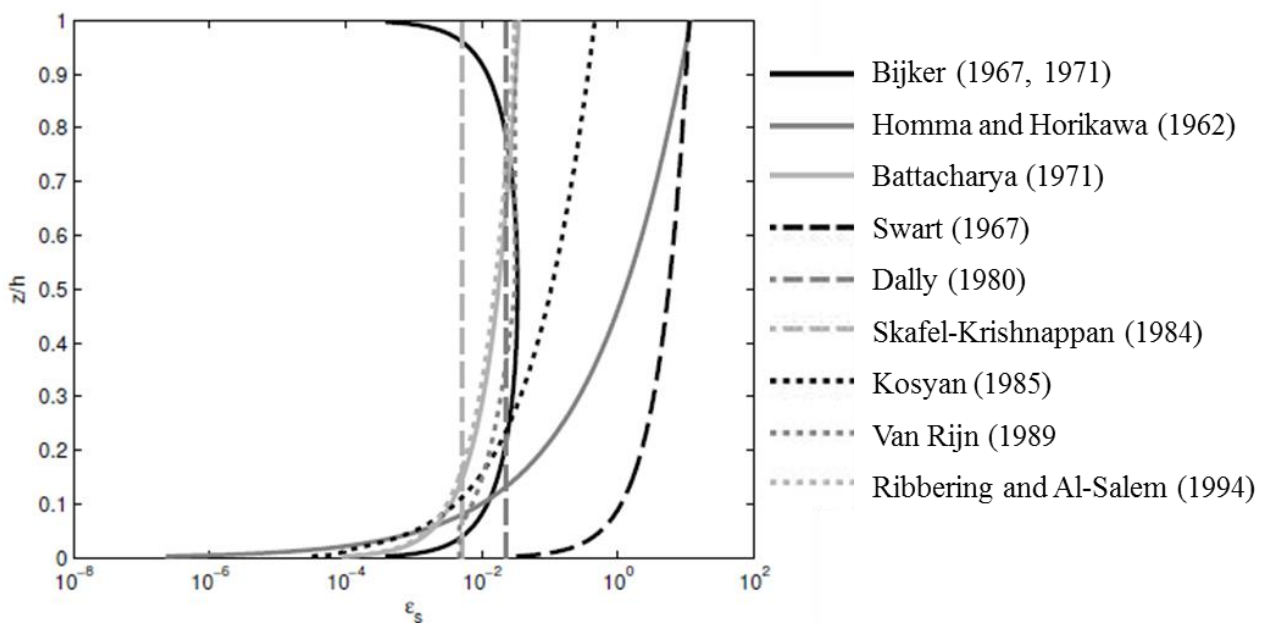


**Figure 39: Overview of sand diffusivity profiles after van Rijn (1993), with $h = 3.5\ m$, $H = 1.5\ m$, , $T = 6.5\ s$, $D_{50} = 137\ \mu m$.**

The exponential law of Ogsten and Sternberg (2002) and the parabolic model developed by Rouse (1937), generally over predict eddy diffusivity values (Figure 30). The linear model from Ogsten and Sternberg (2002) underpredict the eddy diffusivity values (Figure 30). Bose and Dey (2009) solved this problem by adding two extra fit parameters $\alpha$ and $\beta$ in the Rouse calculation of $\epsilon_s$:

$$\epsilon_s = \beta \kappa u_* z_{STM} (1 - \alpha \frac{z_{STM}}{h}) \quad (5.1)$$

By choosing $\beta = 2$, making the friction velocity 2 times larger, model values correspond much better with measured values which are realistic compared to other field studies (e.g. Ogsten & Sternberg, 2002; Thorne et al., 2009). This may have two causes: first, models are not representative for surfzone conditions. Second, calculated friction velocities $u_*$ are underestimated. This study does not focus on the exact calculation of $u_*$, but in future studies this would need more attention to investigate the usage of models for eddy diffusivity calculations.

It is to be expected that eddy diffusivity depends on hydrodynamic parameters and bedforms. For example Thorne et al. (2009) concluded that sand entrainment is controlled by the steepness of ripples. This is also confirmed in a laboratory study by Thompson et al. (2013). In this study, high and steep vertical SSC profiles are correlated with high bed roughness caused by steep ripples. The influence of different ripple types is not reflected in figure 39.b where eddy diffusivities range over all calculated values. Ogsten and Sternberg (2002) found higher eddy diffusivities under broken waves compared to unbroken waves. They explain this by the distance from the breakpoint of the waves. When measurements are closer to the breakpoint, a higher level of mixing can play a role in the water column. This is less visible in this study. For example in figure 29.e-d vertical SSC profiles differ particularly in the amount of sand rather than steepness. The distance to the wave breakpoint could not be accurately measured due to the varying morphology and the constantly changing water depths in the surfzone. The relative wave height gives only an indication for the waves with respect to this breakpoint. Nevertheless, relative wave heights corresponding to the highest sand concentrations fluctuate between 0.35 and 0.6. From this it may be concluded that similar conditions with respect to the wave breaking zone are analyzed in this study. This can be an explanation for the similarities in concentration profiles found during this field campaign.

## 5.3 Tidal asymmetry

An undervalued aspect in this study is the dynamics of bedforms on short time scales. It is assumed that bedforms adjust instantaneously with the highly dynamic hydrodynamics and that the bedforms are in equilibrium with the prevailing hydrodynamics. Actually, ripple formation can lag in time in order of tens of minutes to hours (Osborne & Vincent, 1993; Hanes et al., 2001; Austin & Masselink, 2008). It appeared from flow tunnel experiments by Doucette and O'Donoghue (2006) that ripple geometry is largely independent on the initial bed state. The time to reach equilibrium depends more on the current strength which means that ripples reach equilibrium states faster at strong currents compared to weak currents.

This may be an explanation for the two suspension mechanisms which are divisible based on current Shields parameter (Figure 33). Suspension mechanism 1, sand concentration peaks at falling water, generally experience weak currents. These weak currents have less capacity to change the ripple geometry resulting in bedforms which are not in equilibrium and too big regarding the hydrodynamic conditions in situ. Due to these larger bedforms, larger bed roughness could be generated producing higher sand concentrations than was expected based on hydrodynamics and corresponding equilibrium bed states. Since bedforms are not in equilibrium with the hydrodynamics, also vertical SSC profiles are not in equilibrium because they depend on the bed roughness caused by the bedforms. Vincent and Hanes (2002) call this *history effects* of the bed. They state that this has a considerable effect (factor 2 of more) on the expected suspended sand concentration. Suspension mechanism 2, highest sand concentration occurs at high water, is observed at strong currents only (Figure 33). Bedform reach equilibrium state earlier at strong currents resulting in vertical SSC profiles which quickly respond to changing hydrodynamics and bedforms without any time lag.

Several studies showed that relaxation time in bedform development mainly occurs during the ebb-tide (Austin, et al., 2007). Bedforms can develop gradually to near-equilibrium states at rising tide, but these bedforms are over-developed during falling water when currents are not strong enough to change ripple geometry instantaneously. This tidal asymmetry was also observed by Davidson (et al.,1993). They divided one tidal cycle into three different regimes (Figure 40). They assumed that the wave orbital velocity could be computed by cnoidal wave theory, which is convenient for the prevailing asymmetrical waves in this surf zone region. During the flood phase (region 1, Figure 40), the high wave orbital velocity leads to a sheet flow

regime with high concentration at the bed. In region 2 at high tide, ripples can develop leading to higher sand concentrations in the entire water column. In this region 2, the wave orbital velocity already turns to higher values (around run number 20, Figure 40), while the suspended sand concentration variance increases at falling water (region 3, Figure 40). In this figure, the high sand concentration is correlated to the destruction of the ripple field. Masselink and Pattiaratchi (2000) allocated this concentration asymmetry to the proportionally excessive bed roughness caused by the preserved over-developed bedforms

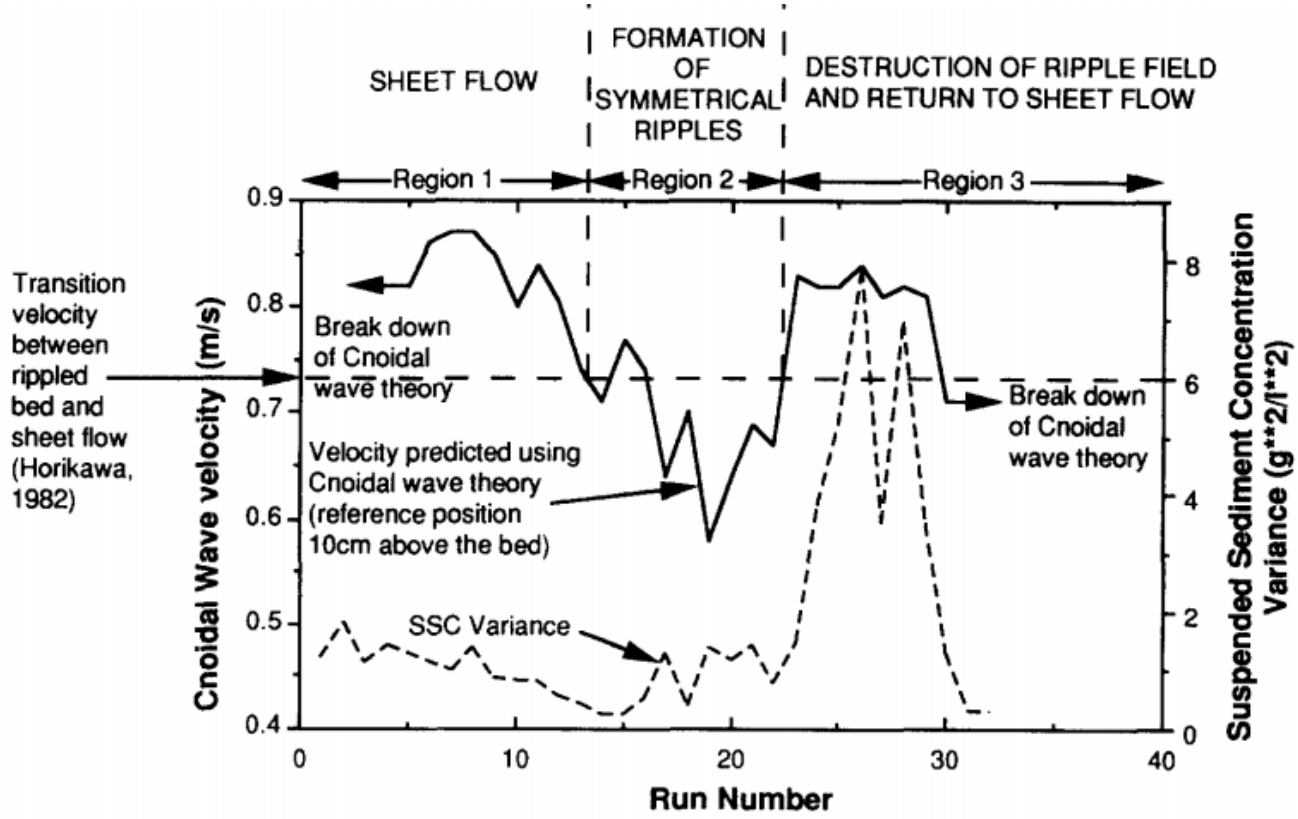


**Figure 40: Variation of total suspended sand variance and cross-shore current velocity with tidal stat (Davidson, et al., 1993).**

# 6 Conclusions

In this thesis the influence of hydrodynamics and bedforms on vertical SSC profiles in the surf zone is investigated under field conditions. Suspended sand concentrations and bed form geometry were measured during a field campaign near Egmond aan Zee in October 2013.
In the surfzone the reference concentration $(C_0)$, which determines the magnitude of suspended sediment concentration, is less dependent on hydrodynamic conditions compared to model studies. The near-bed concentration ranged between $\sim 0.5 - 10\ g/l$ for all hydrodynamic conditions and any bedform type classified. Also no relation between eddy diffusivity values, which determines the steepness of vertical SSC profiles, and hydrodynamics or bedform types could be found. There is not simply one hydrodynamic parameter or one type of bedform which determines the shape and magnitude of suspended sand concentrations. In this study vertical SSC profiles showed the same shape above different type of bedforms and no distinction in suspended sand could be made based on hydrodynamic conditions. This is caused by the fact that ripples are not in equilibrium with the prevailing hydrodynamic conditions. Especially when currents are weak, bedforms can not adjust to smaller bedforms which belong to less energetic conditions. Due to the over-developed bedforms, bed roughness is higher and induce higher sediment concentrations than would be expected based on the hydrodynamic conditions. In higher energetic conditions, bedforms can adjust more easily resulting in high sediment concentrations at the most intense hydrodynamic conditions.

## References


**Aagaard, T. & Hughes, M., 2013.** Sediment transport. In: *Treatise on Geomorphology,* Volume 10, pp 74-105.

**Aagaard, T. & Jensen, S.G, 2013.** Sediment concentration and vertical mixing under breaking waves. *Marine Geology,* Volume 336, pp. 146-159.

**Arnott, R.W. & Southard, J.B., 1990.** Exploratory flow-duct experiments on combined-flow bed configurations, and some implications for interpreting storm-event stratification. *Journal of Sedimentary Petrology,* Volume 60, Issue 2, pp. 211-219.

**Austin, M.J. & Masselink, G., 2008.** The effect of bedform dynamics on computing suspended sediment fluxes using optical backscatter sensors and current meters. *Coastal Engineering,* Volume 55, Issue 3, pp. 251-260.

**Austin, M., Masselink, G., O'Hare, T. & Russell, P., 2007.** Relaxation time effects of wave ripples on tidal beaches. *Geophysical Research Letters,* Volume 34, Issue 34, Article number L16606, doi:10.1029/2007GL030696.

**Bolaños, R., Thorne, P.D. & Wolf, J., 2012.** Comparison of measurements and models of bed stress, bedforms and suspended sediments under combined currents and waves. *Coastal Engineering,* Volume 62, pp. 19-30.

**Bose, S. & Dey, S., 2009.** Suspended load in flows on erodible bed. *International Journal of Sediment Research,* Volume 24, Issue 3, pp. 345-324.

**Camenen, B., 2009.** Estimation of the wave-related ripple characteristics and induced bed shear stress. *Estuarine, Coastal and Shelf Science,* Volume 84, Issue 4, pp. 553-564.

**Camenen, B. & Larson, M., 2008.** A general formula for noncohesive suspended sediment transport. *Journal of Coastal Research,* Volume 24, Issue 3, pp. 615-627.

**Coffey, F.C. & Nielsen, P., 1987.** The influence of waves on current profiles. *Proc. 20th Int. Conf. on Coastal Eng.*, Volume I, New York, U.S.A., Soc. Civ. Engrs., Part I, Chapter 7, pp. 82-96.

**Davidson, M.A, Russel, P.E, Huntley, D.A & Hardisty, J., 1993.** Tidal asymmetry in suspended sand transport on a macrotidal intermediate beach. *Marine Geology,* Volume 110, Issue 3-4, pp. 333-353.

**Davies, A.G. & Thorne, P.D., 2008.** Advances in the study of moving sediment and evolving seabeds. *Surv Geophys,* Volume 29, Issue 1, pp. 1-36.

**Dolphin, T. & Vincent, C., 2009**. The influence of bed forms on reference concentration and suspension under waves and currents. *Continental Shelf Research,* Volume 29, Issue 2, pp. 424-432.

**Dong, L.P., Sato, S. & Liu, H., 2013**. A sheetflow sediment transport model for skewed-asymmetric waves combined with strong opposit currents. *Coatal Engineering,* Volume 71, pp 87-101.

**Doucette, J.S. & O'Donoghue, T., 2006.** Response of sand ripples to change in oscillatory flow. *Sedimentology,* Volume 53, Issue 3, pp. 581-596.

**Grant, W.D. & Madsen, O.S., 1986.** The continental-shelf bottom boundary layer. *Annual Review of Fluid Mechanics,* Volume 1, pp. 265-305.

**Grant, W.D. & Madsen, O.S., 1979.** Combined wave and current interaction with rough bottom. *Journal of Geophysical Research,* Volume 84, Issue C4, pp. 1797-1808.

**Green, M. & Black, K., 1999.** Suspended-sediment reference concentration under waves: Field observations and critical analysis of two predictive models. *Coastal Engineering,* Volume 38, Issue 3, pp. 115-141.

**Hanes, D.M., Alymov, V., Chang, Y.S. & Jette, C., 2001.** Wave-formed sand ripples at Duck, North Carolina. *Journal of Geophysical Research,* Volume 106, Issue C10, pp 22575-22592

**Huisman, C., 2009.** *Sediment concentration and diffusivity profiles under skewed waves from ripples to sheet flow,* Utrecht University: Master Thesis.

**Jayaratne, M.P.R. & Shibayama, T., 2007.** Suspended sediment concentration on beaches under three different mechanisms. *World Scientific,* Volume 49, pp. 357-392.

**Kleinhans, M.G., 2005.** Phase diagrams of bed states in steady, unsteady, oscillatory and mixed flows. In: *Sandpit, sand transport and morphology of offshore sand mining pits,* Aqua publications, paper Q.

**Kobayashi, N., Zhao, H. & Tega, Y., 2005.** Suspended sand transport in surf zones. *Journal of Geophysical Research,* Volume 110, Issue 12, pp. 1-21.

**Lee, G.H., Dade, W.B., Friedrichs, C. T.& Vincent, C.E., 2004.** Examination of reference concentration under waves and currents on the inner shelf. *Journal of Geophysical Research,* Volume 109, Issue 2, pp. 1-10.

**Li, M.Z. & Amos, C.L., 1998.** Predicting ripple geometry and bed roughness under combined waves and currents in a continental shelf environment. *Continental Shelf Research,* Volume 18, Issue 9, pp. 941-970.

**Li, M.Z., Amos, C.L., 1999.** Field observations of bedfroms and sediment transport tresholds of fine sand under combined waves and currents. *Marine Geology,* Volume (158), pp. 147-160.

**Masselink, G., Austin, M.J., O'Hare, T.J. & Russel, P.E., 2007.** Geometry and dynamics of wave ripples in the nearshore zone of a coarse sandu beach. *Journal of Geophysical Research,* Volume 112, Issue 10, Article nuber C10022, doi:10.1029/2006JC003839.

**Masselink, G. & Pattiaratchi, C., 2000.** Tidal asymmetry in sediment resuspension on a macrotidal beach in northwestern Australia. *Marine Geology,* Volume 163, Issue 1-4, pp. 257-274.

**Nielsen, P., 1986.** Suspended sediment concentrations under waves. *Coastal Engineering,* Volume 10, Issue 1, pp. 23-31.

**Nielsen, P., 1992.** *CoastalBottomBoundaryLayersandSedimentTransport.* World Scientific.

**Ogston, A.S. & Sternberg, R.W., 2002.** Effect of wave breaking on sediment eddy diffusivity suspended-sediment and longshore sediment flux profiles in the surfzone. *Continental Shelf Research,* Volume 22, Issue 4, pp. 633-655.

**Osborne, P.D. & Vincent, C.E., 1993.** Dynamics of large and small-scale bedforms on a macrotidal shoreface and breaking waves. *Marine Geology,*Volume 115, Issue 115 (3-4), pp. 207-226.

**Ribberink, J.S., Dohemn-Janssen C.M., Hanes, D.M., McLean, S.R., Cincent, C., 2000.** Near-bed sand transport mechanisms under waves. *Proc. 27th Int. Conf. Coastal Engineering,* Issue Sydney, ASCE, New York, pp. X3263-3276.

**Rouse, H., 1937.** Modern conceptions of the mechanics of turbulence. *Trans. Am. Soc. Civ. Eng. ,* Volume 102, pp. 436-505.

**Schrijvershof, R.A., 2014.** *Bedform morphology under combined wave-current conditions in a nearshore environment,* sl: Master thesis Utrecht University.

**Sistermans, P.G.J, 2002.** *Graded sediment transport by non-breaking waves and a current,* Delft University of Technology, Report No. 02-2, ISSN 0169-6548: Faculty of Civil Engineering and Geosciences.

**Sistermans, P. & Van der Graaff, J., 1999.** The effect of grading on the vertical distribution of suspended sediment. *Coastal sediments,* pp. 48-63.

**Soulsby, R., 1997.** *Dynamics of marine sands.* first red. London: Thomas Telford Publications.

**Thompson, C.E.L, Kassem, H. & Williams, J., 2013.** Nearshore sediment resuspension and bed morphology. *Journal of Coastal Research,*(Special Issue No. 65), pp. 1593-1598.

**Thorne, P.D., Davies, A. G. & Bell, P.S., 2009.** Observations and analysis of sediment diffusivity profiles over sandy rippled beds under waves. *Journal of Geophysical Research,* Volume 114, Issue 2, Article number C02023, doi:10.1029/2008JC004944.

**Thorne, P.D., Williams, J. & Davies, A.G., 2002.** Suspended sediments under waves measured in a large-scale flume facility. *Journal of Geophysical Research,* Volume 107, Issue 8, doi: C8, 3178, 10.1029/2001JC000988.

**Van der Werf, J.J., Ribberink J.S., O'Donoghue, T., Doucette, J.S., 2008.** Modeling of sediment transport processes over full-scale ripples in regular asymmetric oscillatory flow. *Continental Shelf Research,* Volumce 53, Issue 8, pp. 657-673.

**Van Rijn, L.C., 1984.** Sediment transport: part I: bed load transport; part II: suspended load transport; part III: bed forms and alluvial roughness.. *Journal of Hydraulic Engineering,* Volume 110, pp. 1431-56.

**Van Rijn, L.C., 1993.** *Principles of sediment transport in river, estuaries and coastal seas.* Amsterdam, The Netherlands: Aqua Publications.

**Van Rijn, L.C., 2007.** Unified View of Sediment Transport by Currents and Waves. II: Suspended Transport. *Journal of Hydraulic Engineering,* 2007(June), pp. 668-689, DOI: 10.1061(ASCE)0733-9429(2007)133:6(668).

**Van Rijn, L.C., Ribberink, J.S., Van der Werf, J. & Walstra, D.J.R., 2013.** Coastal sediment dynamics: recent advances and future research needs. *Journal of Hydraulic Research,* Volume 51, Issue 5, pp. 475-493.

**Vincent, C. & Hanes, D., 2002.** The accumulation and decay of near-bed suspended sand concentration due to waves and wave groups. *Continental Shelf Research,* Volume 22, Issue 14, pp. 22-14.

**Zheng, J., Li, R.J., Feng, Q. & Lu, S., 2013.** Vertical profiles of fluid velocity and suspended sediment concentrartion in nearshore. *Ineternational Journal of Sediment Research,* Volume 28, Issue 3, pp. 406-412.